The Interstellar Medium Surrounding the Sun

Priscilla C. Frisch,[1] Seth Redfield,[2] and Jonathan D. Slavin[3]

[1]Department of Astronomy and Astrophysics, University of Chicago, Chicago, Illinois 60637; email: frisch@oddjob.uchicago.edu

[2]Astronomy Department, Wesleyan University, Middletown, Connecticut 06459; email: sredfield@wesleyan.edu

[3]Harvard-Smithsonian Center for Astrophysics, Cambridge, Massachusetts, 02138; email: jslavin@cfa.harvard.edu

Keywords

interstellar medium, heliosphere, interstellar dust, magnetic fields, interstellar abundances, exoplanets

Abstract

The Solar System is embedded in a flow of low-density, warm, and partially ionized interstellar material that has been sampled directly by in situ measurements of interstellar neutral gas and dust in the heliosphere. Absorption line data reveal that this interstellar gas is part of a larger cluster of local interstellar clouds, which is spatially and kinematically divided into additional small-scale structures indicating ongoing interactions. An origin for the clouds that is related to star formation in the Scorpius-Centaurus OB association is suggested by the dynamic characteristics of the flow. Variable depletions observed within the local interstellar medium (ISM) suggest an inhomogeneous Galactic environment, with shocks that destroy grains in some regions. Although photoionization models of the circumheliospheric ISM do an excellent job of reproducing the observed properties of the surrounding ISM, the unknown characteristics of the very low-density hot plasma filling the Local Bubble introduces uncertainty about the source of ionization and nature of cloud boundaries. Recent observations of small cold clouds provide new insight into the processes affecting the local ISM. A fuller understanding of the local ISM can provide insights into the past and future Galactic environment of the Sun, and deeper knowledge of the astrospheres of nearby stars.

1. INTRODUCTION

The local interstellar medium (ISM) is the screen through which we view the rest of the Universe. The breakthrough that revealed the pervasive warm, partially ionized "intercloud" gas surrounding the Sun was provided by *Copernicus* data, which for the first time offered access to UV lines that trace the nearest ISM. The discovery that interstellar gas pervades the Solar System was not anticipated. The first observations of the fluorescence of solar Lyα radiation off of interstellar HI inside of the heliosphere were confirmed when Copernicus measurements of the velocity of the Lyα emission linked the interstellar gas inside and outside of the heliosphere. Over the past two decades, high spectral-resolution *Hubble Space Telescope* (HST) data of the ISM toward nearby stars have provided a wide range of information on interstellar clouds close to, and around, the Sun. These data, recent radio and soft X-ray measurements, and detailed theoretical models give a nearly consistent picture of our Galactic neighborhood and provide the context for evaluating the physical properties of the nearest ISM. Over the past two years, the *Interstellar Boundary Explorer* (IBEX) is providing a new level of information about interactions between the ISM and the heliosphere and the interstellar magnetic field, through measurements of the energetic neutral atoms (ENAs) and in situ detections of interstellar helium and oxygen. The dynamical nature and small-scale structure of the ISM close to the Sun guarantee a constantly varying Galactic environment for the Sun, which has a profound impact on the configuration of the heliosphere and flux of Galactic cosmic rays at the Earth.

The ISM that is closest to the Sun is slightly altered by interactions with the solar wind. The interactions between the fast outflowing solar wind and the surrounding ISM, which moves $\sim$26 km s^{-1} relative to the Solar System, results in the complex structure known as the heliosphere (3.2). The heliosphere is the bubble of space that is affected by the solar wind plasma and shaped by interactions with the ISM. The mean free path of interstellar neutrals is on the order of the size of the heliosphere so that, though ions are deflected around the heliosphere by the magnetic field, interstellar neutrals penetrate into the inner heliosphere. Thus, spacecraft in Earth orbit can detect interstellar neutrals and provide valuable information on the nature of the very local ISM.

2. THE GALACTIC ENVIRONMENT OF THE SUN

The local ISM is dominated by the large cavity known as the Local Bubble. This region of very low density extends 50–200 pc in all directions and has even been claimed to extend directly into the Galactic halo (Frisch & York 1983, Welsh et al. 2010a). Large bubbles like the Local Bubble have been seen in many regions in the Galaxy and in external galaxies and are evidence of the powerful role played by massive stars through their stellar winds and clustered supernovae in shaping the ISM. The very low-density ISM that fills the Local Bubble has a direct impact on the physical properties of nearest ISM.

2.1. The Local Bubble

The Local Bubble concept arose from color excess maps showing a hole of dimensions $\sim$50$\times$100 pc (in the Galactic plane) in interstellar dust around the Sun, in conjunction with observations of the diffuse soft X-ray background (SXRB) present over the entire sky. The SXRB, as observed by the low spatial and spectral resolution proportional counters of the Wisconsin Group (McCammon et al. 1983), showed no evidence for energy-dependent absorption of very low-energy X-rays, below 0.2 keV. This suggested that all of the plasma creating this emission was contained within the Local Bubble cavity. As we discuss below, higher spatial and spectral resolution data have since demonstrated that a fraction of the low energy emission is absorbed and so must originate
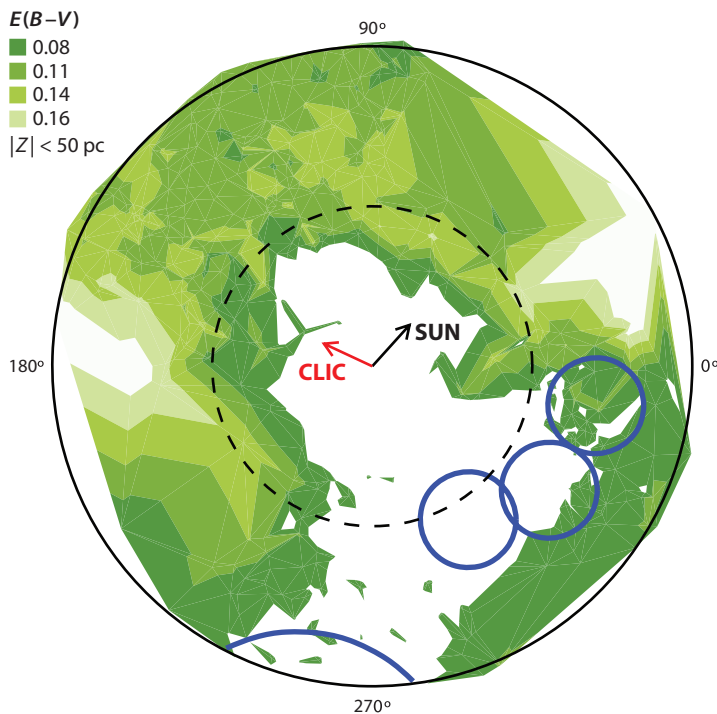
Figure 1

The Local Bubble, as defined by interstellar dust, is shown based on color excess $E(B-V)$ data in the Hipparcos catalog (Perryman 1997). Projected extinctions are shown for stars within 50 pc of the Galactic plane. The local standard of rest (LSR) vector motions of the cluster of local interstellar clouds (CLIC; *red arrow*) and the Sun (*black arrow*) are nearly perpendicular. The best-fitting local interstellar magnetic field (Section 7) overlaps the solar motion in this projection. $E(B-V)$ contour levels of 0.08, 0.11, 0.14, and 0.16 mag correspond to log $N(\text{H\,I}+H_2)$ column densities of 20.65, 20.82, 20.90, and 20.96, respectively, for $N(\text{H\,I}+H_2)/E(B-V) = 5.8 \times 10^{21}$ atoms cm^{-2} mag (Bohlin, Savage & Drake 1978). The locations of the three subgroups of the Sco-Cen Association (*large blue circles*) and Gum Nebula (*arc* centered near $\ell \sim 260°$) are given.

in distant regions. Nevertheless, a cavity filled with extremely low-density gas does exist with its dimensions revealed in a range of data. **Figure 1** shows the cavity "walls" in $E(B-V)$, with the walls corresponding to minimum column densities of $N(\text{H}) > 10^{20.65}$ cm^{-2} (Frisch & Slavin 2006). The cavity walls are also apparent in interstellar H I [for $N(\text{H}) > 10^{18.70}$ cm^{-2}: Paresce 1982, Frisch & York 1983], Na I [for $N(\text{H}) > 10^{19.3}$ cm^{-2}: Sfeir et al. 1999, Welsh et al. 2010a], optical polarization [for $N(\text{H}) > 10^{19.8}$ cm^{-2}: Leroy 1999; Berdyugin, Piirola & Teerikorpi 2004], and in $E(b-y)$ (Vergely et al. 2010).

Such a large, low-density cavity clearly suggests creation by stellar winds or supernova explosions. Several studies relate the Local Bubble with the Scorpius-Centaurus Association, the nearest OB star association. In particular it has been proposed that Loop I expanded into the low-density interarm region between the Sagittarius and Perseus spiral arms (Frisch 1981, 1995; Bochkarev 1987) as a result of sequential star formation over the past 10–15 Myr in the three youngest subgroups of the association (de Geus 1992, Frisch 1995, Maíz-Apellániz 2001). Fuchs et al. (2006) employ an unbiased simulation of the motions of B-stars in the Solar Neighborhood to show that the Local Bubble could have been created by stars in the subgroups of the Scorpius-Centaurus Association entering the present bubble region 10–15 Myr ago.

The first comprehensive interpretation of the low-energy soft X-ray diffuse background was the so-called displacement model, in which uniform emissivity hot gas at $T \sim 10^6$ K was proposed to fill the bubble and is unabsorbed by the neutral gas that was displaced to create the cavity (Snowden et al. 1990). The hot gas was assumed to be in collisional ionization equilibrium, and the intensity variations were explained by the variation in emission path length for the line of sight. A deficit in the expected emission from the Fe line complex at ~72 eV was an early sign of trouble for the model, indicating either that the standard emission model was inadequate or that Fe is depleted by a factor of 3–7 in the hot gas (Bloch, Priedhorsky & Smith 1990; McCammon et al. 2002). The Fe abundance in the gas phase is uncertain, because some interstellar dust may be in the form of robust iron-rich grain cores that survive dust destruction in interstellar shocks (Section 6).

A more serious problem for the displacement model was hinted at by observations within the heliosphere. The observation of soft X-ray emission from comet Hyakutake (Lisse et al. 1996), explained as being generated from charge exchange between solar wind ions and cometary neutrals, led to another possible explanation for the SXRB. It is now clear that a significant contributor to the SXRB derives from foreground emission due to solar wind charge exchange (SWCX) with interstellar neutrals. In this process, highly ionized solar wind ions undergo charge exchange interactions with neutral interstellar H and He flowing into the Solar System, leaving the ions in an excited state that decays by emitting soft X-ray photons (Koutroumpa et al. 2009, Robertson et al. 2010). Questions remain, however, as to the exact flux of the X-rays from SWCX, because of the complexity of modeling the heliosphere (Section 3.2), uncertainties in the atomic physics, and the high degree of variability of the solar wind. Evidently, SWCX accounts for most of the ROSAT 1/4 keV emission for short sightlines in the galactic plane, but more emission is seen at the lowest energies than can be explained by SWCX models, especially in the direction of the heliosphere tail. Although there are still uncertainties in the soft X-ray models, the temperature of the very low-density plasma in the Local Bubble must be $10^{5.65}$–10^6 K, to be consistent with the SWCX emissions and limits on the OVI emission (Koutroumpa et al. 2009), and the emission measure of the Local Bubble plasma must be below values derived ignoring solar wind charge-exchange. Continued work on the SWCX emission and emission processes within the Local Bubble, as well as observations aimed at detecting both the SWCX foreground and cosmic SXRB, will be needed to untangle the sources of the weak diffuse emission.

Because existence of the cavity in neutral gas is not in dispute, the question has become: What fills the Local Bubble? Some plasma within the bubble is needed to confine the nearby clouds, because the clouds do not appear to be expanding. Hot gas has the advantage over warm ionized gas, because the radiative cooling rate is low, reducing the energy requirement to an energetic event sometime in the past several million years. The nature and properties of the hot gas are key to understanding the physical properties of the local ISM because there is a need for a diffuse ionizing radiation field to provide ionization in the complex of LICs (see Section 5). We advocate for the existence of hot gas within the Local Bubble, though with a thermal pressure in the range of $p/k \sim 3{,}000$–$7{,}000$ cm^{-3} K so that it is in pressure equilibrium with the LIC that surrounds the Solar System. We note that the earlier displacement model for the SXRB had a difficulty in that it predicted a thermal pressure, $P/k \sim 15{,}000$ cm^{-3} K, substantially larger than that of the LIC (e.g., Snowden et al. 1998). The lower predicted thermal pressure in the Local Bubble resolves this issue.

2.2. Interstellar Radiation Field

Photoionization plays a major role in the physics of the nearby ISM. The interstellar radiation field must be able to maintain the warm temperatures, $T \sim 6{,}000$–$7{,}000$ K, and partial ionization
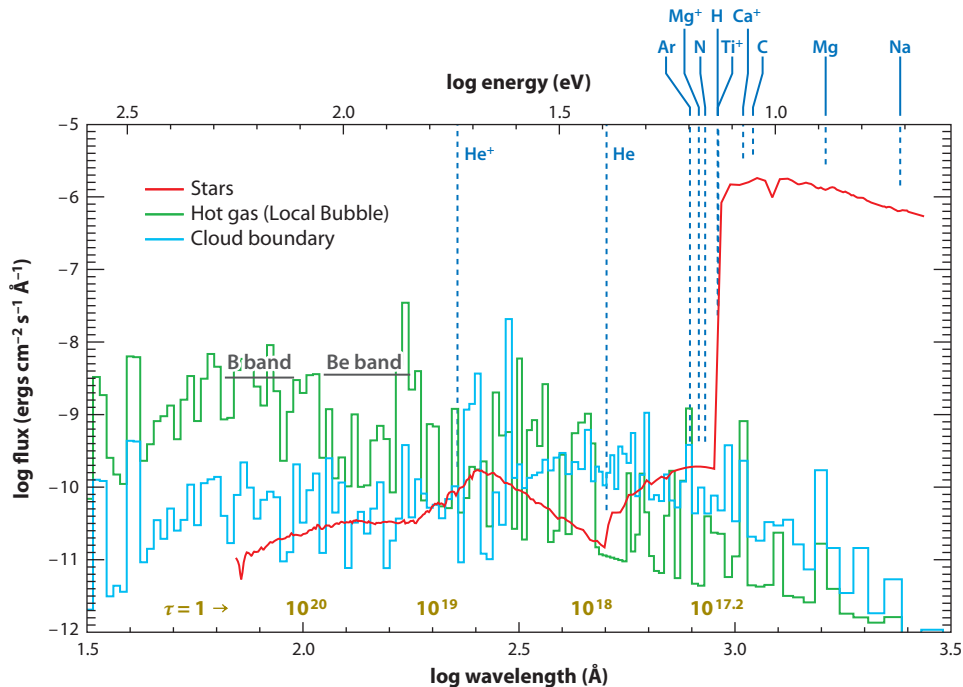
Figure 2

Components of the interstellar radiation field at the Solar location, based on the cloud properties of model 26 by Slavin & Frisch (2008). Fluxes are given as a function of wavelength (bottom X-axis) and energy (top X-axis). The modeled hot Local Bubble gas is the green histogram, whereas the blue histogram shows the emission from a conductive boundary on the LIC. The smooth red line is the stellar extreme-UV/far-UV background. The red numbers above the bottom axis give column densities corresponding to an optical depth of one at that energy/wavelength. The gray bars indicate the bandpasses for the B and Be bands of the Wisconsin group's soft X-ray detectors (McCammon et al. 1983).

of nearby clouds. The most obvious and noncontroversial sources of ionizing flux are nearby stars. The distribution of hot stars within the Local Bubble and its irregular shape creates an inhomogeneous interstellar radiation field near the Sun (e.g., Murthy, Henry & Sujatha 2010). The diffuse spectrum of dust-scattered starlight, which has no correlation with galactic latitude, shows the spectrum of an early B star. All of the stronger (and less absorbed) stellar extreme-UV sources have been observed by the all-sky survey of the *Extreme Ultraviolet Explorer* (EUVE). The softer part of the EUV interstellar radiation field is especially inhomogeneous because the radiation field is dominated by the two B stars, β CMa and ϵ CMa (Adhara), located inside the Local Bubble in the third galactic quadrant. Although there are other B stars within the Local Bubble, their location and the intervening HI column prevents them from ionizing the LIC, and they were not seen in the EUVE all-sky survey. Many white dwarfs exist within the Local Bubble, and HZ 43, G191-B2B, and Feige 24 contribute strongly to the EUV flux observed at shorter wavelengths. In **Figure 2**, we show the various components of the interstellar radiation field that ionize the local ISM, including the observed stellar flux and the modeled diffuse soft X-ray and EUV emission. Vallerga (1998) has shown that the stellar ionizing radiation field can provide a large fraction of the ionization of H in the LIC, but not all of it. In addition, the stellar radiation field falls far short of explaining the observed ionization of He (see Section 4.3.2).

Because of the highly anisotropic EUV interstellar radiation field, we expect that an ionization gradient should exist in the nearby ISM, though the complexities of shadowing of clouds by other clouds, and the integration over lines of sight with varying ionization conditions, can obscure such effects. We discuss ionization modeling in Section 5 and note that the nearby clouds are not optically thick in the EUV in general, nor very optically thin, and thus are expected to have at least H ionization gradients internally in addition to cloud-to-cloud variations. The far-UV (FUV) radiation field, responsible for ionizing the low first ionization potential elements such as C, Mg, S, and Fe, is not absorbed by neutral H and, thus, can travel over much longer distances in the ISM. The main opacity source in the FUV is dust. As a result, the interstellar radiation field at FUV wavelengths is composed of the flux of many A and B type stars. The interstellar radiation field at $\sim$975 Å (Opal & Weller 1984) should be similar to the field at 1,045 Å that ionizes CaII. The 975 Å radiation field is highly asymmetric, with 96% of the flux at the Sun from B and O stars in Gould's Belt in the longitude interval of 180°–360°.

2.3. Loop I and S1 Shell

The local ISM may have been substantially affected by the Loop I superbubble shell. Loop I was detected first as a giant radio continuum loop in the Northern Hemisphere, 160° in diameter and centered near $\ell, b = 330°, 5°$ (Heiles 1998). Loop I is a morphologically distinct filamentary HI shell; such shells typically have $B_{\parallel} \sim 6.4$ μG, hydrogen column densities of $N(HI) > 10^{21}$ cm^{-2}, and small ratios of thermal to magnetic pressure, $\beta p \sim 0.1$ (Heiles 1989). On the order of 5% of disk gas volume is in shells (Kalberla & Kerp 2009). The soft X-ray emission from Loop I has been modeled as a reheated supernova remnant in Upper Scorpius $\sim$250,000 years old (see reviews by Cox & Reynolds 1987, Frisch 1995). Radio filaments at distances of $\sim$80 pc shadow the X-ray emission (Egger & Aschenbach 1995), and create the appearance of a boundary between Loop I and Local Bubble that, however, is not supported by detailed mapping of the interstellar magnetic field in this region (Santos, Corradi & Reis 2010). The proposal that the Loop I shell expanded asymmetrically into the low-density region around the Sun (Frisch 1981) is supported by the preference for HI shells to expand into interarm regions (McClure-Griffiths et al. 2002). All Loop I models place the Sun in or near the rim of the shell (e.g., Heiles 1998).

The high-latitude polarized radio continuum intensities at 1.4 GHz show two different magnetic field directions that have been modeled by Wolleben (2007) as originating from the compression of magnetic fields in two expanding spherical superbubble shells. These features, the S1 and S2 shells, are part of Loop I and have magnetic field directions that differ by $\sim$90° $\pm$ 40°. Optical polarizations of stars within 40 pc give a magnetic field direction close to the Sun that is consistent with the field direction in the S1 subshell (Frisch 2010). The locations of the S1 and S2 shells converge in several nearby regions for the assumed spherical geometry (see Section 8.2). If these shells are spherical, they must dominate the ISM close to the Sun (see Section 4.2.3), and in any case the kinematics of ISM within 40 pc is consistent with the properties of the S1 shell (see Section 4.2). The Wolleben picture contrasts with models of a more distant interaction region between the current configurations of Loop I and the Local Bubble (Section 9) so that the evolved S1 and S2 shells would have to be older than the filamentary structures now separating the two features.

3. SOURCES OF DATA ON THE VERY LOCAL INTERSTELLAR MEDIUM

A rich and diverse variety of data are available on the local ISM, including interstellar absorption lines, as well as in situ measurements of the ISM and the products formed from the interaction

between interstellar neutrals and the solar wind. We introduce the term cluster of local interstellar clouds (CLIC) to refer to the interstellar clouds within ∼30 pc that are flowing past the Sun. Data-constrained heliosphere models provide a source of information on the circumheliospheric ISM (CISM).

3.1. High-Resolution Spectral Data

The richest source of information on the properties of the nearby ISM are high spectral resolution optical and UV absorption line observations of sight lines toward the nearest stars. High-resolution HST data are supplemented by medium-resolution FUV data from FUSE (*Far Ultraviolet Spectroscopic Explorer*), IMAPS (Interstellar Medium Absorption Profile Spectrograph), and *Copernicus*. At the ∼3 km s^{-1} resolution possible with the HST spectrographs, the number of interstellar components fit to the absorption lines of the refractory elements MgII and FeII is relatively constant for stars within 30 pc and increases weakly for stars at 30–40 pc (figure 14 in Redfield & Linsky 2004a), suggesting that most of the absorbing ISM is close to the Sun. Therefore, certain stars at distances of ∼100 pc can provide data on the ISM within a few parsecs, such as ϵ CMa (132 pc; Gry & Jenkins 2001). For example, the two clouds toward Sirius, 2.7 pc away and close to the ϵ CMa sightline, are at the same velocities and have similar characteristics as those toward ϵ CMa. A similar perspective emerges from DI data toward stars within 45° of the Galactic plane with $\ell > 90°$; N(DI) rises with distance for stars within 13 pc and shows no significant rise on the average for stars with distances of 13–30 pc. Ionization and gas-phase abundances affect the absorption lines that trace this component structure.

Measurements from a single absorption line provide the Doppler-shifted cloud velocity, velocity dispersion, and ISM column density. The symmetric Gaussian-like profiles seen for unsaturated absorption lines support the fundamental assumption that these absorbers represent individual ISM clouds. The standard analysis of absorption lines rely on a Voigt profile to approximate an absorption feature that is broadened by several independent phenomena (van de Hulst & Reesinck 1947). The mass-dependent temperature and mass-independent turbulence act, in principle, as separate broadening mechanisms that together give the line width, which is expressed as the Doppler broadening parameter $b^2 = \frac{2kT}{m} + \xi^2$, where m is the particle mass, T is the temperature, k the Boltzmann constant, and ξ is the turbulent velocity.

The assumption that thermal broadening provides the only mass-dependent contribution to line widths may be invalid if a turbulent magnetic field significantly accelerates the ions. Comparing turbulence in interstellar plasma to turbulence in the solar wind, Spangler, Savage & Redfield (2010) concluded that there is no evidence for anisotropy of the velocity fluctuations or temperature, nor Larmor-radius-dependent heating in the observations of the nearest interstellar clouds. This result relies on the mass-independent turbulent velocity values obtained from the Voigt profile assumption.

In principle the cloud physical properties such as temperature, microturbulence, ionization fraction, relative abundances, dust depletion, and electron densities can be determined by combining the mass-dependent velocity information for different ions and neutrals in the same sight line. Of course, not all interstellar absorbers have the same column densities or internal physical properties, so line diagnostics vary from cloud to cloud. Elements and ions observed in the nearby clouds by HST include HI, DI, CI, CII, CII*, CIV, NI, OI, AlII, SiII, SiIII, SiIV, MgI, MgII, SII, and FeII. High-resolution ground-based data of the local ISM include CaII and NaI. FUSE, *Copernicus*, and IMAPS provide additional data on CIII, NII, NIII, and ArI. With data from many sight lines, the 3D morphology and kinematics can be studied, enabling investigations of fundamental questions of the origins, evolution, and interaction of nearby clouds.

LICs have such low column densities ($\log N_{\mathrm{H}} = 17.0 - 18.5$ cm^{-2}; Redfield & Linsky 2004a) that only the 100 strongest atomic transitions are useful for sampling cloud properties (figure 2 of Redfield 2006). The spectral distribution of sensitive lines strongly favors the shortest wavebands, with 69% in the FUV, 28% in the UV, and 3% in the optical. The clouds close to the Sun appear to have a common kinematic driver (Section 4), resulting in closely spaced velocity components, typically ≤ 10 km s^{-1}, where multiple components are present in a sightline (see figure 2 of Linsky, Rickett & Redfield 2008).

The strong transitions available in the UV ensure that local ISM detections are made along all sight lines, even the shortest (i.e., αCen; Linsky & Wood 1996). Approximately 60 sight lines within 30 pc have UV observations [see compilations of Redfield & Linsky (2002, 2004a) and Wood et al. (2005)]. FUSE observations of FUV lines are available for nearby white dwarf stars (e.g., Jenkins et al. 2000, Lehner et al. 2003). Due to their brightness in the optical and a relatively smooth continuum caused by rapid rotation, hot stars are typically targeted in optical local ISM observations. However, many nearby targets are cool stars with stellar emission lines underlying interstellar absorption lines. Analyzing the interstellar absorption overlaying the stellar continuum often requires modeling a self-reversed stellar emission feature, especially for the HI Lyα feature that cannot be measured without foreground ISM attenuation (e.g., Wood et al. 2005). Because these features are variable for stars with active chromospheres, multiple observations during different phases of the stellar activity cycle would yield more accurate data for the absorption components toward some cool stars.

Ground-based observations have the advantage that very high-resolution and ample observing time are available, but the disadvantage that only the ionization states of CaII and NaI, as well as TiII, are useful for local ISM studies. For example, in the 6,400 K partially ionized CISM, only 1.6% of the gas-phase calcium is singly ionized, whereas only 0.15% of the sodium is neutral (**Table 1**). Despite the small number of accessible transitions in the optical, the ease of making observations and high spectral resolution still makes optical data a valuable source of data for understanding the local ISM.

Table 1 Model results for ionization fractions[a] in the ISM at the heliosphere

Element	PPM	I	II	III	IV
H	10^6	0.776	0.224	–	–
He	10^5	0.611	0.385	4.36(–3)	–
C	661	2.68(–4)	0.975	0.0244	0.000
N	46.8	0.720	0.280	8.52(–5)	0.000
O	331	0.814	0.186	4.71(–5)	0.000
Ne	123	0.196	0.652	0.152	2.79(–6)
Na	2.04	1.47(–3)	0.843	0.155	6.34(–6)
Mg	6.61	1.98(–3)	0.850	0.148	0.000
Si	8.13	4.21(–5)	0.999	8.02(–4)	3.10(–5)
S	15.8	6.47(–5)	0.971	0.0288	1.95(–6)
Ar	2.82	0.263	0.500	0.238	2.83(–6)
Ca	4.07(–4)	9.21(–6)	0.0155	0.984	1.87(–4)
Fe	2.51	7.01(–5)	0.975	0.0245	5.75(–6)

[a]Numbers less than 10^{-2} are written as $x(y)$, where y is the exponent and x is the mantissa (or significand). These results are taken from model 26 of Slavin & Frisch (2008).

3.2. The Interstellar Medium Inside of the Heliosphere

The ISM inside of the heliosphere and the interaction between the heliosphere and surrounding interstellar gas and dust provide unique diagnostics of the velocity, temperature, composition, and gas-to-dust ratio in the surrounding ISM. We introduce a new acronym, the CISM, because of the need to uniquely identify the circumheliospheric gas and dust entering the heliosphere from the ISM. Until recently, the ISM surrounding the Sun was thought of as part of the LIC, but that name has been reused (Section 4.2) to identify an expanded set of absorption components with a velocity that may, or may not (Section 3.2.1), be consistent with the velocity of interstellar neutral He inside of the heliosphere that by definition is the velocity of the CISM.

The interaction between the ISM and the heliosphere also provides baseline information for understanding the astrospheres of exoplanetary systems (Section 10). The ~ 26 km s^{-1} motion of the Sun through the ISM creates an elongated heliosphere (the solar wind bubble) shaped by the ram pressure of the solar wind and circumheliospheric interstellar cloud. The heliosphere varies with the magnetic activity cycle of the Sun, as well as with the outer boundary conditions set by the density, ionization, temperature, velocity, and interstellar magnetic field in the surrounding ISM (see individual articles in Frisch 2006). The angular offset between the upwind direction of the interstellar flow through the heliosphere and the interstellar magnetic field direction add an additional asymmetry to the heliosphere.

The heliosphere itself either has a classic two-shock or a one-shock structure (Zank 1999). Moving outward from the Sun, the first heliosphere landmark is the solar wind termination shock, at ~ 95 pc in the upwind direction, where the supersonic solar wind plasma becomes subsonic. The solar wind in the outer heliosphere is mass-loaded by ions created by charge-exchange with denser interstellar neutrals. We note that the distance to the termination shock is variable both in space and time as demonstrated by the Voyager 1 and 2 crossings of the shock. The heliopause, which is the contact discontinuity between the inflowing ISM and the subsonic solar wind plasma, is half-again more distant. In the upwind direction, the inner heliosheath between the termination shock and heliopause has temperatures of $\sim 10^6$ K, whereas the outer heliosheath just beyond the heliopause has temperatures of $\sim 5 \times 10^4$ K (Richardson & Stone 2009). Neutral interstellar atoms with first ionization potentials similar to H I charge-exchange with protons as they traverse the heliosheath regions, partially deflecting and isotropizing a monodirectional flow in a process known as filtration (Müller & Zank 2004). An outer bow shock is expected for the surrounding ISM temperature $\sim 6,340$ K, interstellar magnetic fields ≤ 2.7 μG and ion densities > 0.06 cm^{-3}. A standing bow wave rather than a bow shock should exist if the motion of the Solar System through the surrounding cloud is submagnetosonic.

3.2.1. Velocity vector of interstellar helium. The velocity vector of interstellar He I entering the heliosphere is given by direct measurements of He I atoms, and the fluorescence of backscattered solar 584-Å emission from the He I (Möbius et al. 2004). Less than $\sim 2\%$ of the interstellar He I is lost due to filtration in heliosheath regions (references for filtration are given in table 1 of Slavin & Frisch 2008). The He I is ionized by photoionization and electron impact within 1 AU of the Sun. The measured velocity of interstellar He I is sensitive to both its filtration while crossing the inhomogeneous heliosheath regions, and its latitude-dependent ionization during the 25-year trip to the inner heliosphere. Such effects are relevant to the interpretation of the He-I measurements by IBEX. The velocity is determined primarily from the Ulysses in situ measurements, because the uncertainties on He-I velocities derived from the fluorescence of solar 584 Å radiation are five times larger than those of the in situ data (Möbius et al. 2004). The vector motion for He-I corresponds to a heliocentric velocity of 26.3 ± 0.4 km s^{-1}, toward $\ell = 184°$, $b = -15°$, which is 9° away from,

and 1.8 km s^{-1} slower than, the mean bulk flow of the CLIC past the solar location (Section 4.2). Preliminary results from the IBEX-LO in situ samples of interstellar HeI in the inner heliosphere suggest an interstellar flow vector a few kilometers per second slower than the Ulysses value, and with a slightly different upwind direction (E. Möbius and M. Bzowski, private communication; Möbius et al. 2009). The density of HeI at the termination shock is n (HeI) $= 0.015$ cm^{-3}, and filtration is less than several percent. The nose of the heliosphere is typically defined as the upwind direction of interstellar HeI flowing into the heliosphere (Witte 2004, Möbius et al. 2009). The heliosphere nose does not correspond to the region of the highest plasma compression, which is offset below the upwind HeI direction by $\sim$15° (Section 3.3), because of the angle that the interstellar magnetic field makes with the upwind velocity vector. It is a persistent puzzle that the ISM at the HeI velocity is not seen toward the nearest stars in the upwind direction (Section 4.2), and the Ulysses value given above may yet be superseded.

3.2.2. Interstellar dust. Interstellar dust grains have been measured flowing through the heliosphere (Mann 2009). Included in this population are large micron-sized interstellar dust grains with radii $\sim$1 μm and mass $\sim 10^{-10}$ gr. The size distribution in these large grains is inconsistent with typical interstellar extinction curves (Draine 2009). However, similar micron-sized grains create emission (coreshine) at 3.6 μm from the cores of molecular clouds (Pagani et al. 2010). The best fit to the upwind direction of the interstellar dust detected by *Ulysses* and *Galileo*, for data collected before 2000, is toward the ecliptic coordinates $\lambda = 259° \pm 14°$, $\beta = 8° \pm 3°$ [1-σ uncertainties, $(\ell, b) = (8°, 14°)$; Frisch et al. 1999]. The 5° difference between the interstellar inflow determined from the *Ulysses* HeI and dust data is within the 1-σ errors, but could also reflect unrecognized uncertainties in either the dust or the HeI direction.

3.2.3. Constraining interstellar neutral densities with heliospheric data. In contrast to interstellar ions, interstellar neutrals are able to enter the heliosphere. Astronomical data typically provide the properties of interstellar clouds averaged over the cloud length. However, because of the opacity of the ISM and uneven distribution of ionizing sources (Section 2.2), the absorption line data sample regions where ionization levels may vary by factors of 10–30% or more (Section 5; Wolff, Koester & Lallement 1999). Information on neutrality of the ISM at a single location in space therefore supplies an important constraint on ISM properties (Section 5.3).

Elements that are partially ionized in the CISM (**Table 1**) feed interstellar neutrals, such as H, He, N, O, Ne, and Ar, into the heliosphere where they are ionized (Rucinski et al. 1996) and picked up and convected outward by the solar wind. Magnetic turbulence isotropizes the pickup ion velocity distribution in the rest frame of the solar wind to create the characteristic pickup ion velocity distribution that is flat, extends to a cutoff of twice the solar wind velocity, and has a suprathermal tail.

Pickup ions give the neutral composition of the surrounding ISM. Of special importance is HeI, which enters the heliosphere and experiences minimal ionization in outer regions, providing a useful diagnostic of the CISM neutrality at a single location. Early measurements of the fluorescence of solar photons from interstellar HI and HeI led to predictions that a population of energetic ions should be found in the inner heliosphere that formed from the ionization of interstellar neutrals (Fisk, Kozlovsky & Ramaty 1974). Measurements of the pickup ion composition, after corrections for ionization propagation, and filtration, give the composition of interstellar neutrals at the solar wind termination shock (Gloeckler & Fisk 2007). After corrections for filtration in the outer heliosphere regions, neutral densities in the CISM are obtained.

Helium is gravitationally focused downwind of the Sun. The HeI density in the focusing cone varies between ∼0.01 cm^{-3} (solar maximum) and ∼0.045 cm^{-3} (solar minimum) compared to the interstellar value of 0.015 cm^{-3} at the solar wind termination shock. During solar maximum, the density of the He focusing cone is a factor of ∼2 higher than the HeI density within 1 AU of the Sun on the upwind side, whereas during minimum it is a factor of ∼4 more dense (Frisch et al. 2009).

Anomalous cosmic rays are formed from accelerated pickup ions (e.g., Cummings, Stone & Steenberg 2002), though the acceleration site is not definitively known at present. They provide additional information on interstellar neutrals in the CISM. The isotopic composition of anomalous cosmic rays suggests that the reference abundance for the CISM is solar. Isotopic ratios of Ne, N, and O in the anomalous cosmic rays population have been found to be in better agreement with the Solar System ratios than cosmic ray ratios, with $^{15}N/^{14}N \sim 0.0037$, $^{18}O/^{16}O \sim 0.002$, and $^{22}Ne/^{20}Ne \sim 0.073$ (Leske 2000). Because these isotopes are created from interstellar neutrals, the implication is that the ISM and solar compositions (Asplund et al. 2009) are similar. Isotopic abundances are an important tracer of ISM origin, so further studies would be valuable.

3.2.4. Energetic neutral atoms, the *Interstellar Boundary Explorer* Ribbon, and the interstellar magnetic field.

Charge exchange between interstellar hydrogen and the solar wind and pickup ions creates ENAs (energetic neutral atoms) that provide a new remote diagnostic of plasmas that are mixed with neutrals. IBEX (McComas et al. 2009b) recently mapped ENAs with energies of ∼0.01–6 keV across the sky and discovered a striking nearly complete arc of ENA emission with fluxes ∼2–3 times the distributed emission (McComas et al. 2009a). This feature, which has been dubbed the IBEX Ribbon, has its center located at $\ell, b = 33^0, 55^0$. Comparisons between the Ribbon and heliosphere models capable of predicting known heliosphere asymmetries (Section 3.3) showed that the Ribbon forms in sightlines that are perpendicular to the direction of the interstellar magnetic field draping over the heliosphere. As such, the IBEX Ribbon becomes a powerful tool for understanding the direction of the interstellar magnetic field at the solar location (Section 7).

3.3. Magnetohydrodynamic Heliosphere-Interstellar Medium Models and the Interstellar Magnetic Field

A sophisticated synergy has arisen between observations of ISM inside and outside of the heliosphere and the magnetohydrodynamic (MHD) multifluid heliosphere models that connect them into a self-consistent picture. Theoretical efforts to model heliospheric data such as the IBEX Ribbon, the observed offset between interstellar HI and HeI flowing into the heliosphere, and the 10 AU difference in the crossing of the solar wind termination shock by the Voyager 1 and 2 spacecraft, require knowledge of the ISM that sets the heliosphere boundary conditions. Important ISM properties are the interstellar neutral and ion densities in the CISM and the ISM velocity and magnetic field vectors. The synergy arises because the heliosphere models need accurate boundary conditions to match data, so those models become a test of the ISM boundary conditions of the heliosphere. Especially important is that the heliosphere models provide the best possibility for establishing the strength of the local field. The ISM ram pressure, magnetic field strength and direction, and neutral fractions play different roles in setting the heliosphere configuration. Interstellar HI tends to symmetrize the heliosphere via mass-loading through charge-exchange with ions inside of the heliopause (the contact discontinuity between interstellar and heliospheric plasmas), whereas the interstellar magnetic field, which makes an angle of roughly 45° with respect to the HeI velocity vector, distorts the heliosphere (Washimi & Tanaka 1996; Ratkiewicz, Ben-Jaffel

& Grygorczuk 2008; Izmodenov 2009; Opher et al. 2009; Pogorelov et al. 2009; Heerikhuisen et al. 2010). Comparisons between the interstellar magnetic field from heliosphere models and polarization observations of the nearest stars also can permit detection of small-scale turbulence in the field. The strength of the field inferred from the heliosphere models ranges from 1.8–4.5 μG, for proton densities of n (HII) $= 0.05$–0.07 cm^{-3}. Ultimately, combining the results of MHD heliosphere models with theoretical models that predict the heliosphere boundary conditions from astronomical data (Section 5) will be a powerful tool for understanding the physical properties of the ISM surrounding the heliosphere.

4. CHARACTERISTICS OF THE INTERSTELLAR MEDIUM FLOW PAST THE SUN

In this section, we discuss the dynamics, temperatures, turbulence, and overall ionization levels of the very local ISM. Ultimately, corrections for the partially ionized states of these clouds are required, as has been done for the LIC (Section 5), in order to obtain the gas and dust compositions (Section 6).

4.1. Cloud Column Densities, Temperatures, and Turbulence

The principal sources of data on the properties of clouds close to the Sun are the column densities, temperatures, and turbulence values found from interstellar absorption lines. The most complete set of data on column densities, temperature, and turbulence in the local ISM is the Redfield & Linsky (2004b) analysis of absorption components in the HST database. The results of this ongoing study include:

- A comprehensive database on the distribution of neutral ISM near the Sun, from DI and HI Lyα lines (Redfield & Linsky 2004a, Wood et al. 2005). The mean local column densities toward stars within 10 pc, log N(HI) $= 17.91 \pm 0.18$ cm^{-2}, corresponds to an opacity to H-ionizing radiation of $\sim$3.8, which explains the partially ionized nature of the local ISM. For low column density gas in the Local Bubble [N(HI) $< 10^{19}$ cm^{-2}], the DI/HI ratio is $1.56 \pm 0.4 \times 10^{-5}$ (Linsky et al. 2006).

- The CLIC consists of warm ISM. The weighted mean temperature and turbulence for clouds in the CLIC are, respectively, $6{,}680 \pm 1{,}490$ K and 2.24 ± 1.03 km s^{-1}. The uncertainties do not allow a uniform temperature for all local clouds, which range from 2,000–12,000 K (Redfield & Linsky 2004b).

- The temperature of the cloud anticorrelates with cloud turbulence (Redfield & Linsky 2004b, their figure 3). Redfield & Linsky argue that the origin of the $T-\xi$ anticorrelation may be associated with pressure equilibrium and that it represents a true anticorrelation between the thermal and turbulent pressures (the latter given by $\rho\xi^2$, where ρ is the mass density). Given the anticorrelation between turbulent velocity and temperature, the constancy between thermal and turbulent pressure is pretty good. The correlation coefficient is -0.47 (-1 would be a perfect anticorrelation), in which there is a 0.01% chance that they were drawn from an uncorrelated parent distribution.

- Column density does not correlate with either temperature or turbulence for the highest quality data subset.

- The mean thermal pressure in this population of clouds is $P/k = 2{,}280 \pm 520$ K cm^{-3}, where k is the Boltzmann constant, which is significantly below the nominal pressure of the low-density Local Bubble hot plasma (Section 2.1). If a high value for the pressure in the Local Bubble were true, a strong magnetic field, >6 μG, would be needed to support the cloud against collapse. Turbulent pressure is relatively insignificant (**Table 2**). Such large

Table 2   Properties of warm local interstellar clouds

Property	Value[a]	Comments[b]
CLIC outside of the heliosphere		
Temperature	6,680 $\pm$ 1,490 K	CLIC, AL
Turbulent velocity	2.24 $\pm$ 1.03 km s^{-1}	CLIC, AL
HC velocity magnitude	28.1 $\pm$ 4.6 km s^{-1}	CLIC, AL
HC velocity direction	192°, −11°	CLIC, AL
LSR velocity magnitude	16.8 $\pm$ 4.6 km s^{-1}	CLIC, AL
LSR velocity direction	155°, 5°	CLIC, AL
Log mean H I column density	17.18 $\pm$ 0.70 cm^{-2}	CLIC, AL
H I/He I	14.7 $\pm$ 2.0	CLIC, AL
Electron volume density	0.06–0.21 cm^{-3}	LIC, AL
Electron volume density	0.05–0.08 cm^{-3}	LIC, Models
Thermal pressure (P_T/k)	3,180$^{+1850}_{-1130}$ K cm^{-3}	$P_T = nkT$
Turbulent pressure (P_ξ/k)	280$^{+200}_{-180}$ K cm^{-3}	$P_\xi = \rho\xi^2$
Magnetic field direction	$\ell = 38°, b = 23°$ ($\pm 35°$)	CLIC
Magnetic field direction	$\ell = 33°, b = 55°$	IBEX
Cloud diameter	∼2.5 pc	LIC, AL
Cloud mass	0.32 $M_\odot$	LIC, AL
Interstellar He I inside of the heliosphere		
Temperature	6,300 $\pm$ 340 K	LIC
Velocity magnitude	26.3 $\pm$ 0.4 km s^{-1}	Section 3.2
Velocity direction	184°, −15°	Section 3.2
Volume density	0.015 $\pm$ 0.002 cm^{-3}	LIC[c]

[a]Velocity vectors are in either the heliocentric (HC) or local standard of rest (LSR) reference frame. Conversion to the LSR is made with the solar apex motion of Schönrich, Binney & Dehnen (2010), which gives a solar motion through the LSR of $V_{sun} = 18.0 \pm 0.9$ km s^{-1}, toward $\ell = 47.9° \pm 3.0°, b = 23.8° \pm 2.0°$.

[b]CLIC (cluster of local interstellar clouds) = average of several CLIC sightlines; LIC (local interstellar cloud) = quantity for LIC material only; AL = derived from absorption line (AL) observations; HS = derived from in situ observations inside of the heliosphere (HS).

[c]This He I volume density for the LIC assumes negligible He I filtration in the heliosphere.

field strengths, however, are inconsistent with inferences on the very local magnetic field strength in current MHD heliosphere models (Section 3.3).

Tiny cold dense clouds with median kinetic temperature values of ∼300 K and column densities of ∼10^{18}–10^{19} cm^{-2} are widespread in our Galactic neighborhood (Begum et al. 2010). The striking discovery of Na I absorption lines formed in cold gas within 12–24 pc toward Leo expands the range of cloud physical properties that require explanation (Meyer et al. 2006). Haud (2010) has isolated over ∼1,340 narrow Gaussian components from cold clouds detected by Leiden-Argentina-Bonn H I 21-cm database. A group of cold clouds forms an arc over 90° long, or ring, in the sky, parts of which are nearby and coincides with Na I absorption components toward Leo (Peek et al. 2011). The Na I kinetic temperature and the H I spin temperature are both ∼20 K.

4.2. Kinematics of Interstellar Medium Close to the Sun

Observations of ISM inside of the heliosphere and toward the closest stars show that a wind of clumpy ISM is blowing past the Sun. Although the mean absolute velocity in the LSR for the

absorption components in the wind, 17.9 ± 5.1 km s^{-1}, overlaps the velocities of the high-latitude cold and warm HI in the Arecibo Millennium survey, 11.7 ± 12.7 km s^{-1} (Heiles & Troland 2003), the CLIC velocities are in the range of intermediate velocity clouds. When NI is observed in intermediate velocity clouds, it is generally dynamically associated with NII and SiIII, which is consistent with formation in the partially ionized gas in postshock cooling regions where high CaII/NaI ratios are also found. The high-ratio CaII/NaI∼1 detected toward α Oph (14 pc away) led to the suggestion that the high CaII abundances are due to grain destruction in shocks.

4.2.1. Bulk motion of the cluster of local interstellar clouds. One of the most fundamental results of the kinematics of nearby ISM is that it can, to the first order, be described by a single bulk flow vector (**Figure 3**). Thus, despite being distributed in spatially distinct collections of material, all absorbers are moving with roughly the same speed and in the same direction. This suggests a common kinematic driver and serves as one of the key observational constraints on any theory of the origins and evolution of local ISM. The bulk flow vector of the local ISM through the LSR is a robust result. Based on a combination of CaII, DI, and HI data toward 60 stars, Frisch, Grodnicki & Welty (2002) obtained a bulk flow heliocentric velocity for the CLIC of -28.1 ± 4.6 km s^{-1}, from the direction $\ell = 12.4°$, $b = 11.6°$. This corresponds to a streaming velocity through the LSR of -16.8 km s^{-1} arriving from the direction $\ell \sim 335°$, $b \sim -7°$ (using the solar apex motion given in **Table 2**). **Figure 3** shows clear evidence of deceleration of flow at the leading edge of
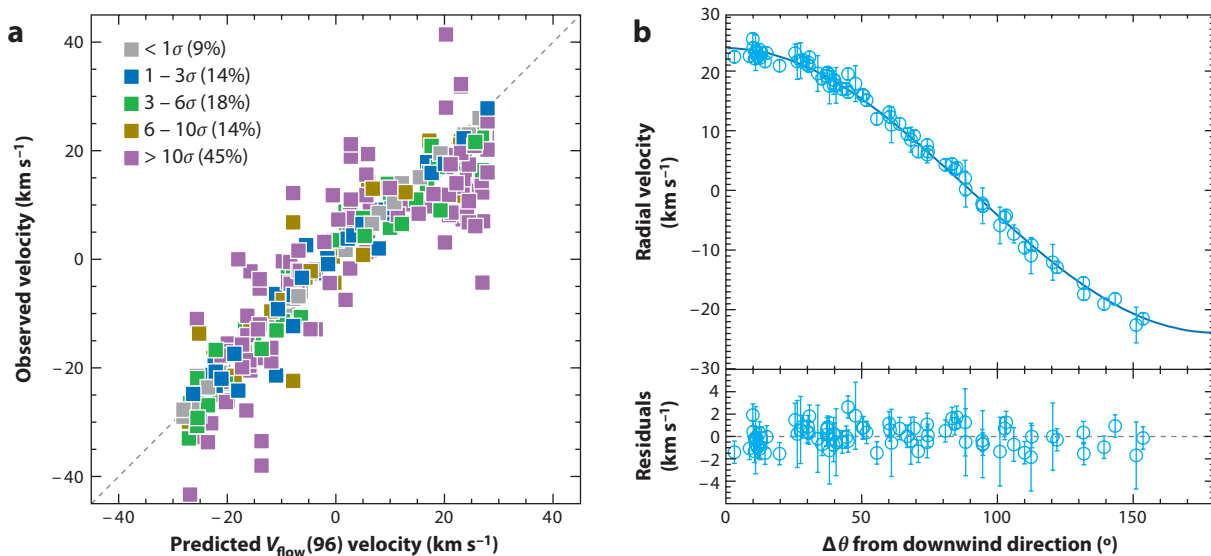
Figure 3

(*a*) Observed velocities of interstellar absorption components in the cluster of local interstellar clouds (CLIC) are plotted against the best-fitting velocity vector for bulk motion of the CLIC (using V_{96} in Frisch, Grodnicki & Welty 2002). In general the agreement is excellent. However, in detail more than 77% of the components differ by more than 3σ from the bulk motion. The deceleration of the local flow is clearly visible between the upwind gas (negative velocities) and downwind gas (positive velocities). These distinct groups of velocity components have motivated several searches for interstellar structures with mutual kinematics. (*b*) Observed radial velocities for absorption line components identified with the local interstellar cloud (LIC) versus the angular distance from the downwind direction. The solid dark-blue curve shows a solid body motion model. The residuals for the data compared to the model are shown in the lower panel. The good fit of the motion to a solid body model suggests that the LIC is a quiescent cloud. Note that these velocities are heliocentric and not in the local standard of rest.
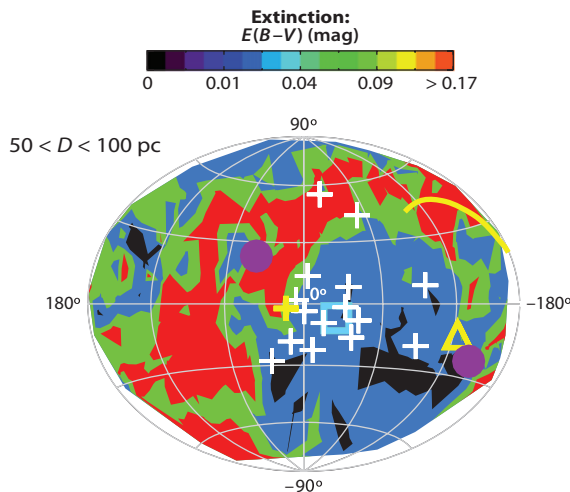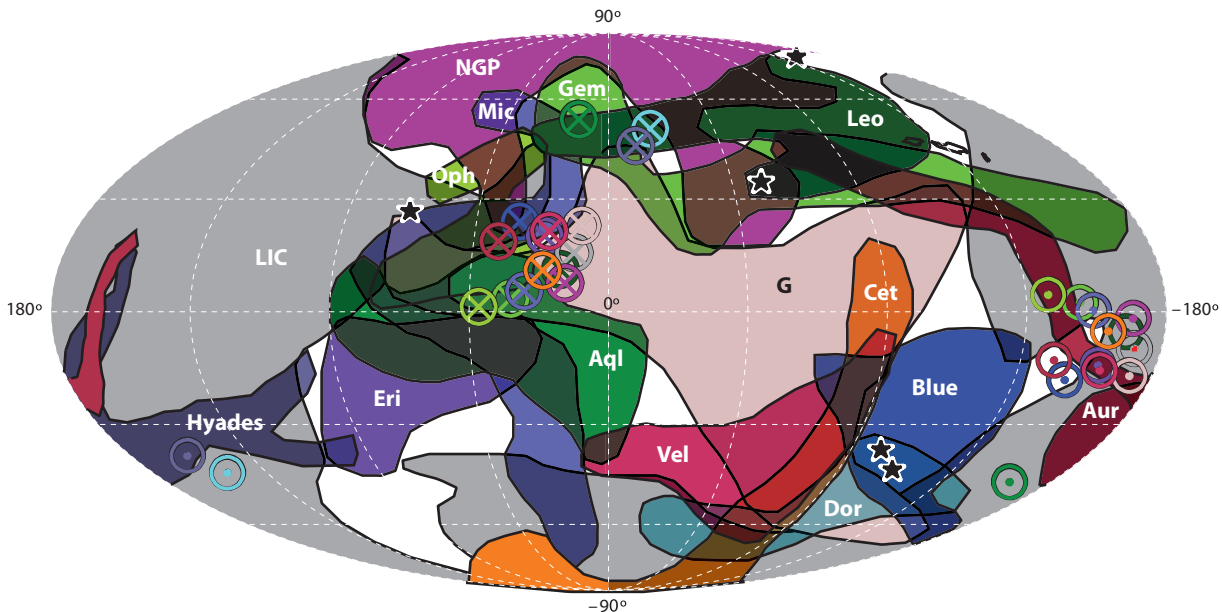
Figure 4

Contours of color excess E(B–V) for stars 50–100 pc from the Sun. The white crosses show the local standard of rest (LSR) upwind directions for the 15 local interstellar clouds identified by Redfield & Linsky (2008). The yellow cross shows the direction of the velocity vector (21.0 km s^{-1}) of the bulk motion of the tiny, cold H I ring (Haud 2010). The cyan-blue square shows the LSR upwind direction of the cluster of local interstellar clouds flow (Frisch, Grodnicki & Welty 2002). The yellow line segment indicates cold, tiny, nearby interstellar clouds seen in Na I and H I (Section 8.2). The yellow triangle gives the center of the ring, toward $\ell, b = 236°, -13°$. The purple dots give the poles of the best-fitting interstellar magnetic field to very local optical polarization data (Frisch et al. 2010a). The regions of lowest E(B–V) in the third galactic quadrant correspond to the brightest regions in the sky at 975 Å (Section 2.2).

the complex of local clouds, corresponding to the downwind direction toward the third galactic quadrant.

4.2.2. Kinematics of local tiny cold clouds. The LSR motion of the H I ring containing the arc of cold clouds that traverses the constellation of Leo near the Sun (Section 4.1) corresponds to an LSR velocity vector of 21.0 km s^{-1} moving toward $\ell, b = 193°, 2°$. This arc of cold gas evidently shares the general motion of the CLIC, but it also rotates and expands rather than moving through space as a rigid body (Haud 2010; **Figure 4**).

4.2.3. Modeling the cluster of local interstellar clouds with 15 clouds. It soon became apparent that deviations from the bulk flow vector were also spatially correlated, providing further evidence that the ISM in the immediate vicinity of the Sun is comprised of a collection of distinct cloud structures. The kinematics of local clouds have been identified and investigated in several different studies that use absorption line measurements of Ti II (Crutcher 1982), Ca II (Frisch & York 1986; Lallement, Vidal-Madjar & Ferlet 1986; Vallerga et al. 1993), and various UV and optical lines (Bzowski 1988; Lallement & Bertin 1992; Frisch, Grodnicki & Welty 2002; Frisch 2003; Redfield & Linsky 2008) to separate velocity components into individual clouds.

In the most complete model yet of the structure of local clouds, Redfield & Linsky (2008) formed a database of 270 absorption components toward stars at distances up to 100 pc and used it to derive a set of 15 clouds, with self-consistent velocities, and that accounted for 80% of the observed absorption components. The fit of components attributed to the feature they identify as the LIC is shown in **Figure 3**. The broad variation between positive and negative velocities is the
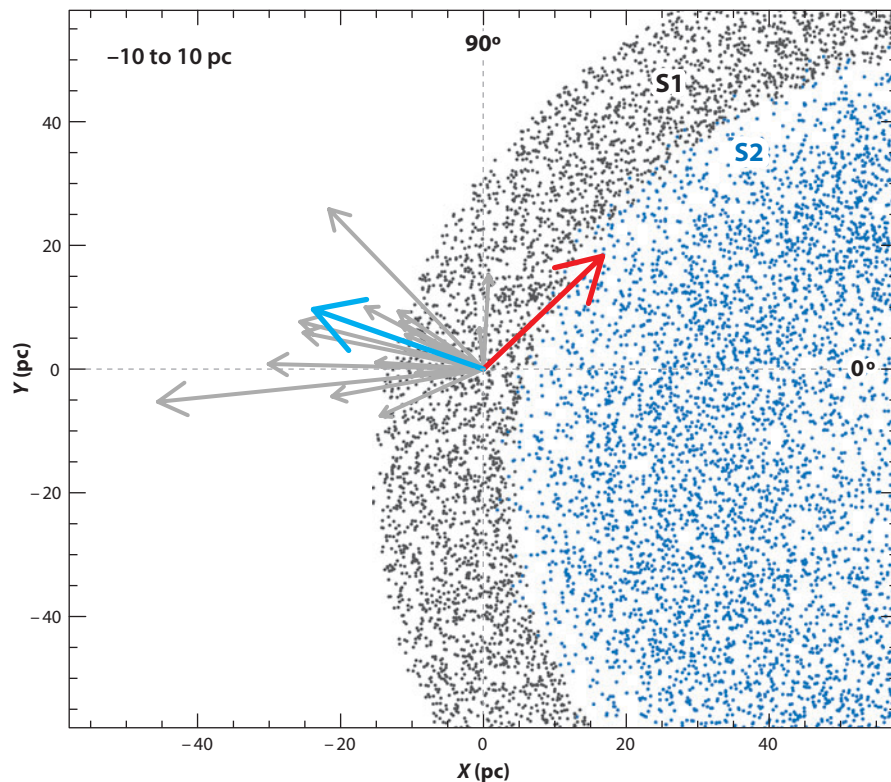
Figure 5

The morphologies of 15 clouds, within 15 pc, determined from absorption lines toward 157 stars 1.3–100 pc away by Redfield & Linsky (2008). Triangulation of the velocity of each cloud provides the primary basis for identification. The heliocentric upwind velocities are labeled with circled X's, whereas downwind directions are labeled with circled dots. The star symbols indicate sight lines of radio scintillation sources in Linsky, Rickett & Redfield (2008). Some of the clouds are named after the constellations toward which they are observed, e.g., Oph, Leo, Cet, Vel, Aql, Eri, Mic, Aur, Dor, and Gem. The other clouds are the Local Interstellar Cloud (LIC), the G-cloud in the Galactic center hemisphere, the North Galactic Pole (NGP) cloud, and the Blue cloud. Hyades denotes the stellar cluster containing many of the stars that sample that cloud.

Doppler effect as the sightline sweeps from downwind (positive velocities) to upwind (negative velocities) directions. The lower panel of **Figure 3b** shows typical deviations of 2 km s^{-1} from the best-fitting vector, with components in the upwind hemisphere favoring slightly blue-shifted velocities compared to the best-fitting vector. Depletions vary by a factor of ten in the feature denoted the LIC. Many of these 15 entities overlap clouds that have been identified in earlier studies. The cloud distances are set by the nearest star showing the cloud and vary from 1 pc to 15 pc, indicating that these clouds dominate the immediate solar galactic environment. From comparisons between the data and simulations of randomly distributed clouds, Redfield & Linsky (2008) concluded that the volume-filling factor of warm clouds within 15 pc is ~6–19%. For sightlines where more than one cloud is identified, differential velocities between clouds are up to 50 km s^{-1} when the 3D cloud motions are utilized (Linsky, Rickett & Redfield 2008). The clouds are shown in **Figure 5**. **Figure 6** shows the cloud velocity vectors in the LSR, projected onto the galactic plane and in comparison to the locations of the S1 and S2 shells (Section 2.3). In the heliocentric and LSR velocity frames, respectively, the mean velocity of these clouds is 33.7 km s^{-1} and 22.9 km s^{-1}, and maximum angular spread between the velocity vectors of the clouds is 71° and 120° (see **Table 2** for the LSR transformation). In either case, the angular spread in the upwind direction for this set of clouds does not suggest a tightly collimated ISM flow.

4.2.4. Which cloud surrounds the Sun? Of the suite of clouds in the nearby ISM, two dominate the sky, the LIC, originally identified as the ISM surrounding the Solar System, and the G cloud

The distribution of interstellar medium in the rim of the S1 (*dark gray*) and S2 (*blue*) magnetic subshells of Loop I, based on the model by Wolleben (2007). Shell configurations are shown for points within ± 10 pc of the galactic plane. The arrows show the vector motions through the local standard of rest of the Sun (*red*), and the cluster of local interstellar clouds (*light blue*). For more details, see Frisch (2010).

that is seen toward the nearest star αCen. The LIC identified in the Redfield & Linsky (2008) model is not detected in all directions, consistent with the original Lallement & Bertin (1992) LIC, although the new LIC is somewhat slower ($\sim$2 km s^{-1}). The heliocentric velocities of the G and LIC clouds differ by 5.8 km s^{-1}, but the directions differ only by $\sim$7°. The small spatial scales of the LIC and G cloud indicate that the Sun transitions these features over geologically short timescales. The limit on interstellar material at the LIC velocity toward the upwind star 36 Oph, is N(HI) $< 6 \times 10^{16}$ cm^{-2} (Wood, Linsky & Zank 2000), giving a distance to the upwind edge of $<$0.1 pc for a cloud density of n (HI) $\sim$ 0.2 cm^{-3}, which the Sun would traverse in 4,000 years. Based on the LIC velocity, the low column densities of the downwind star Sirius and a model placing the cloud velocity parallel to a normal to the LIC surface (giving an interstellar magnetic field direction approximately parallel to the cloud surface), Frisch (1994) estimated that the Sun entered the LIC within the past 10^4 years.

The question as to which interstellar cloud can be identified as the CISM depends on the measured velocity of interstellar HeI inside of the heliosphere (Section 3.2). The CISM is clearly part of the CLIC flow through space (Section 3.2), but the original velocity vector determined for the LIC (Lallement & Bertin 1992) coincided with an earlier, now obsolete, value for the vector motion of HeI inside of the heliosphere (Witte 2004). The HeI velocity of 26.3 ± 0.4 km s^{-1} (Section 3.2) differs by $\sim$3σ from the new LIC velocity of 23.8 ± 0.9 km s^{-1} and is midway between the LIC velocity and the upwind G cloud velocity of $-$29.6 ± 1.1 km s^{-1}. It is unclear whether the Sun is currently inside of the LIC or whether the CISM is part of a transition zone between the LIC and the G cloud. The alternative is that the prevailing value for the HeI vector is incorrect (Section 3.2). A local deceleration of $\sim$3–4 km s^{-1} per parsec is suggested by the

upwind cloud distance of 1 pc, because the G cloud is also seen toward αCen at 1.3 pc. If the Sun should transit between clouds, it would take ISM from the next cloud ~25 years to travel from the heliopause to the Earth. The IBEX Ribbon (Section 3.2.4) is expected to vary once the Sun enters the G cloud, and would provide advance notice of such an event (Frisch et al. 2010b).

4.2.5. Moving scintillation screens. In contrast to absorption line observations that measure the radial velocity of the absorbing cloud, observations of refractive radio scintillation give an estimate of the transverse motion of the scintillating screen. Recently, fast (i.e., hour timescale), high-amplitude, variability of high-redshift quasars has been linked to a scintillation screen within 1–30 pc of the Sun. The velocity vectors of the CLIC (Redfield & Linsky 2008) are a much better fit to the observed transverse flow than the LSR (Linsky, Rickett & Redfield 2008), indicating a clear link between the CLIC and electron density fluctuations causing the radio scintillation. Scintillation screens trace fluctuations in electron density over scales of 10^8 cm through ~0.01 AU. The axial ratios of these features transverse to the sightline are larger than unity, e.g., ~6 in some sightlines. For the local screens, this implies elongated magnetic structures where the ratios of thermal to magnetic pressures are $\beta_P < 1$ (Rickett 2007).

4.3. Evidence for Ionization Variations in the Cluster of Local Interstellar Clouds

The low opacity of the CLIC combined with an inhomogeneous radiation field from stars, the Local Bubble hot plasma, and evaporative cloud interface regions, lead to variations in the ionization levels of the CLIC.

4.3.1. Methods for obtaining electron densities from carbon and magnesium. Over long sightlines in the ISM, the mean electron density can be found from pulsar dispersion measures and Hα emission measures. This method obviously cannot be used to determine the electron density in the local ISM, so data on ionization-sensitive absorption lines toward nearby stars are required. The two most useful electron density diagnostics for the CLIC are the collisionally excited CII* λ1335 fine-structure lines and the MgI λ2852 absorption feature that is enhanced by dielectronic recombination in the temperature range of the CLIC (York & Kinahan 1979, Redfield & Falcon 2008, Slavin 2009). Both techniques yield cloud-averaged electron densities that are based on temperature-dependent rate constants, which behave differently with temperature variations.

Electron densities derived from the ratio CII/CII* must cope with the saturation of the CII 1,335 Å line, resulting from high CII abundances and large atomic oscillator strength. A variety of methods have been used to approximate the CII column density (see Slavin & Frisch 2006, Redfield & Falcon 2008), the most viable being to use S as a proxy for C, because S is typically undepleted in low density, tenuous clouds. This is done by using observations of the SII $\lambda\lambda$ 1253.81,1259.52-Å line and employing an assumed C/S abundance ratio. Electron densities based on the collisionally excited fine-structure lines do not depend on the radiation field, and for warm low-density regions, collisions with neutrals can also be ignored.

The second method of obtaining electron densities from the equilibrium between MgI and MgII requires knowledge of the radiation field near 1,600 Å, which is fairly well known (Section 2.2). The dielectronic recombination cross section for MgII $\rightarrow$ MgI, for the temperature range 5,000–10,000 K, increases sharply with temperature while the radiative recombination rate slowly decreases. These rates are difficult to measure in the laboratory for this temperature range, so sophisticated models of coupling between atomic levels are required. (See the Atomic Data and

Analysis Structure (ADAS) database or the Oak Ridge Controlled Fusion Atomic Data Center, available at **http://www-cfadc.phy.ornl.gov/data_and_codes**).

The ratios MgII/MgI and CII*/CII define separate ranges of allowed values for the electron densities that will overlap at the true value. Using these techniques, an electron density for nearby clouds is found to be in the range from $\sim$0.01–1.0 cm^{-3} with a mean of $\sim$0.1 cm^{-3} and a standard deviation of $\sim$0.04 cm^{-3}. In particular, Redfield & Falcon (2008) find for their sample $n_e = 0.11^{+0.10}_{-0.05}$ cm^{-3}. The interstellar electron density in the CISM that is derived from the photoionization models is $\sim$0.06–0.07 cm^{-3} (Section 5.3).

4.3.2. Helium ionization. In regions where He is partially ionized, the electron and proton densities are not equal because of the high He ionization. The relative ionization of H and He diagnoses the strength and hardness of the ionizing radiation field, because the first ionization potentials are at 13.6 eV and 24.6 eV, respectively. Observations of absorption of stellar EUV flux by the EUVE satellite, from both neutral H and He, have provided some of the most direct data on H and He ionization. Although it was not unexpected that H should be partially ionized because of the nearby white dwarfs and a few B stars, a big surprise in the data was the high value for the ratio of HI/HeI. Even the hottest stars ionize H more than He, so H/He ratios are expected to be less than the cosmic abundance ratio, A(H)/A(He) $\approx$ 10. On the contrary, however, the HI/HeI ratio was found to be generally greater than 10 with an average value of $\sim$14 (Dupuis et al. 1995), indicating that He is more ionized than H in the CLIC. All of the stellar EUV sources important for ionizing the LIC were observed by EUVE, and it was found that the ionizing spectrum from them falls far short of being able to account for this level of He ionization (Vallerga 1998). Therefore, there must either be an additional source of hard ionizing photons responsible for the He ionization (and some of the H ionization) or the gas must be out of photoionization equilibrium and overionized for its temperature.

There is evidence for variation in ionization for different clouds, which can be attributed to variation in the EUV radiation field as well as possibly different cloud histories and densities. This is not surprising in that even a low column density cloud, e.g., N(HI) = 2×10^{17} cm^{-2}, is optically thick near the H ionization edge so clouds similar to the LIC will cast shadows that can strongly affect the ionization of other clouds. As an example, Holberg et al. (1999) determined a value for the ratio N(HI)/N(HeI) of 7.4 for the line of sight toward the white dwarf REJ1032+532, whereas the mean value found by Dupuis et al. (1995) was 14 for the six white dwarfs they observed (also using EUVE).

Based on the [HeI]/H$_\alpha$ emission ratios in the warm ionized medium (WIM), Reynolds (2004) found that the He ionization levels are similar in the WIM and LIC, or 30–60% versus $\sim$40% (using the results of Slavin & Frisch 2008). In contrast, by comparing Hα with the forbidden [OI] λ 6,300 line, Reynolds found that the ionization of H in the WIM is significantly larger than the $\sim$24% level in the LIC, leading to the suggestion that the interstellar radiation field is harder in the LIC than globally. The EUVE data are consistent with the local radiation field, because Wolff, Koester & Lallement (1999) found no systematic gradient in the He ionization levels of $\sim$40%. However, there is recent evidence that dust scattered H$_\alpha$ can provide 50% of the high-latitude H$_\alpha$ emission (Witt et al. 2010), and the effects of this scattered light on the ionizing spectrum of HI are not yet clear.

4.3.3. Nitrogen ionization. An additional piece of evidence regarding the ionization level in the CLIC comes from the ionization level of N because it has an ionization potential close to H and is tied to the H ionization by charge transfer (though not so closely as O). Observations of NI and NII, for example with FUSE (Lehner et al. 2003), IMAPS, and *Copernicus* (Frisch et al. 2011,

in preparation), found substantial ionization of N on most lines of sight. The ratio NII/NI varies between 1.0 ± 0.14 in the -3.8 km s^{-1} component toward η UMa [and HZ 43, of the North Galactic Pole (NGP) cloud, Section 4], and 1.38 ± 1.26 toward HD 149499A (37 pc away and located toward the center of Loop I). Wood et al. (2002) found an NII/NI ratio for the Capella line of sight to be $\sim 0.58 \pm 0.82$. For comparison, model 26 by Slavin & Frisch (2008) predict NII/NI $= 0.39$ for the CISM at the solar location. Variations of the strength and hardness of the interstellar radiation field over the ± 37-pc volume indicated by these data is likely to explain this ionization variation. Evidently, the CISM is more sheltered from high levels of 13.6-eV radiation compared to these nearby high-latitude clouds and regions closer to the center of Loop I.

5. MODELING THE CIRCUMHELIOSPHERIC INTERSTELLAR MEDIUM AND THE LOCAL INTERSTELLAR CLOUD

Much of the nearby ISM consists of partially ionized diffuse gas. The mean column density from HI Lyα absorption toward stars within 10 pc is log N(HI) $= 17.91 \pm 0.18$ cm^{-2} (Wood et al. 2005), so that cloud opacities at the HI ionization potential, 13.6 keV, are on the order of $\tau \sim$ 3–8. Whether this gas is in photoionization equilibrium and the nature of the ionizing radiation field are of central importance to interpreting the ionization indicators for obtaining accurate abundances from ions formed in both neutral and ionized gas and to the thermal balance of these clouds. Within the photoionization equilibrium model for local ISM by Slavin & Frisch (2008), the hot gas plays important roles in directly providing ionizing radiation, but especially in causing the evaporation of the cloud via thermal conduction. It is actually the radiation from the evaporative interface between the warm cloud gas and the hot gas that produces most of the diffuse radiation that ionizes the interstellar HeI close to the Sun. Models of the flux from evaporative boundaries confirm that an adequate level of photoionization occurs for the local ISM, even when the soft X-ray flux assumed for the hot gas is reduced to a level that is consistent with the SXRB after the foreground SWCX emission (Section 2.1) has been removed.

### 5.1. Support for Ionization Equilibrium

An important piece of evidence regarding the ionization equilibrium in local ISM has been provided by observations of the ArI 1,048.2 Å line with IMAPS (Jenkins et al. 1996) and FUSE (e.g., Lehner et al. 2003). Neutral argon is a valuable diagnostic because Ar is unlikely to be significantly depleted from the gas phase in the warm ISM and because the Ar$^\circ$ photoionization cross section is 5–30 times larger than the H$^\circ$ cross section, whereas the Ar$^+$ recombination coefficient is of the same order of magnitude as that of H$^+$ at the temperature of the CLIC clouds. Sofia & Jenkins (1998) and Jenkins et al. (2000) argue that if ArI/HI is significantly below the cosmic abundance of Ar, then the ionization of Ar must be controlled by photoionization; whereas if the observed ratio is close to the cosmic abundance ratio, then recombination from an overionized state is determining the ionization of Ar and nonequilibrium ionization is important. The finding by Jenkins et al. (2000) that, for lines of sight toward four nearby stars, the N(ArI)/N(HI) ratio is below its B star abundance ratio value by a factor of roughly -0.4 dex tells us that photoionization plays a dominant role in the ionization of Ar. Detailed calculations of nonequilibrium ionization suggest that fractional ionization of Ar and H are similar until after the gas is cooled and photoionized (Slavin 2009). We have tested whether a compromise situation could exist in which a photoionizing background radiation field could increase the Ar ionization and, yet, the gas is still out of ionization equilibrium. Such a model is of interest because ions other than Ar could conceivably have significant nonequilibrium effects even though the ionization of Ar is dominated by

photoionization. We find that the timescale for ArI/HI to reach the observed ratio is long, governed by the recombination timescales for Ar^+ and H^+, and as a result other ions are essentially at their equilibrium ionization.

5.2. Ionization Gradients in the Local Interstellar Cloud

In many regions in the ISM, an assumption of either high ionization, via a strong stellar ionizing source, or low ionization, because the cloud is very optically thick, is adequate for modeling the ionization. In the CLIC, this is generally not the case because the radiation field is weak and the cloud column densities are small, typically with $N(HI) \leq 10^{18.5}$ cm^{-2}. Under these conditions, the clouds, and the LIC in particular, are partially ionized and have significant ionization gradients, at least for some elements, between the edge of the cloud and its deepest parts. This is illustrated in **Figure 7** for H, He, Ar, and Ne. In this situation, one needs to perform radiative transfer calculations in order to derive the ionization throughout the cloud, thus allowing the calculation of ionization corrections and gas-phase elemental abundances both in the cloud and at entry to the heliosphere. For the purposes of understanding the ionization levels of the ISM that creates the heliosphere boundary conditions, we have the additional information about neutral densities provided by data on these neutrals inside of the heliosphere (Section 3.2). The photoionization models for the CISM require assembling the initial interstellar radiation field (Section 2.2) and self-consistently determining the ionization, heating, and cooling throughout the cloud (Slavin & Frisch 2008).
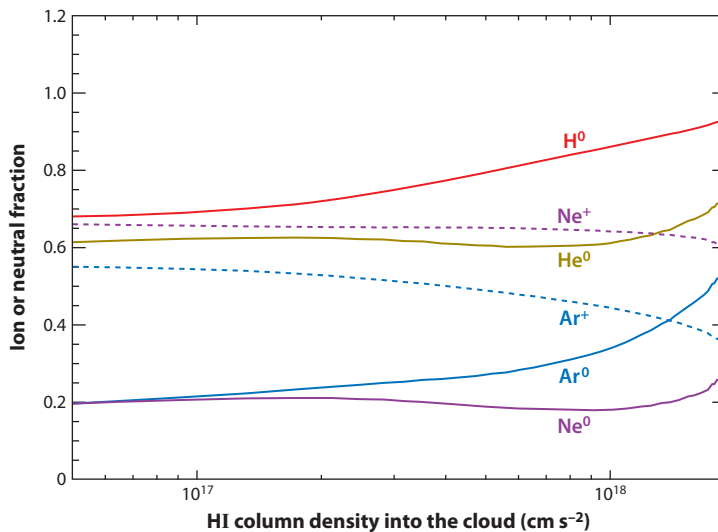
Figure 7

Ionization as a function of depth (HI column density) into the cloud for H, He, Ar, and Ne as calculated for model 26 by Slavin & Frisch (2008). The cloud surface is at 0 (*left*) and the solar location for this model is at 4×10^{17} cm^{-2}. The substantial variation in ionization of H is evident, while the He ionization level is fairly constant. Both the conductive boundary on the local interstellar cloud and hot stars contribute to the ionizing radiation field (**Figure 2**). Solid lines show the ionization fractions of the neutrals for the elements as listed in the legend, whereas the dashed lines show the ionization fractions for singly ionized Ne and Ar. Both of these elements have significant twice-ionized fractions.

5.3. Photoionization Equilibrium Models of the Circumheliospheric Interstellar Medium

Photoionization models for the LIC (Slavin & Frisch 2008) provide the ionization corrections required to recover accurate abundances from partially ionized ISM. The absorption line data, in conjunction with the models, can then provide constraints on the gas-phase abundances of the elements. Model results for the interstellar fractional ionizations are shown in **Table 1**. These ionization results are for one point in the cloud, namely the location just outside the heliosphere. For several abundant elements the approximation of one dominant ion stage is valid; for example C, Si, S, and Fe are all more than 97% singly ionized. In contrast, H, He, N, and O are divided between neutral and singly ionized states. Other elements have significant ion fractions in three ionization states, e.g., Ne and Ar. The well-observed ions NaI and CaII are both trace ionization stages and, thus, sensitive to small variations in the ionizing radiation field (Frisch 2010). The combination of MgI, MgII, CII*, and SII data argues for a supersolar C abundance in one sightline (Slavin & Frisch 2006), though other sightlines yield different interpretations (Redfield & Falcon 2008).

The radiative transfer calculations show that when ions are mainly ionized by the EUV radiation field, their ionization state varies significantly with depth into the cloud (**Figure 7**). For this reason, finding a common model for both absorption line and in situ data requires a radiative transfer calculation. In addition, the ionization in the ISM just outside of the heliosphere is an important input and boundary condition for numerical MHD models of the heliosphere.

5.3.1. Unusual constraints on cloud ionization.
Through the ratio HI/HeI, the densities of interstellar HeI inside of the heliosphere are an important constraint on cloud ionization at the location of the Sun. The pickup ions provide additional unique information on the densities of neutral atoms in the CISM, including He, N, O, and Ne (together with Ar from anomalous cosmic rays). Pickup ions are the primary method for measuring the interstellar NeI density in the CLIC. The predicted densities for NeI and ArI in the CISM, based on interstellar Ne and Ar abundances of 123 ppm and 2.82 ppm, respectively, agree with pickup ion Ne and Ar abundances at the termination shock for minimal filtration of Ne and Ar (filtration values are summarized in table 1 of Slavin & Frisch 2008). Once filtration is better understood, the combination of photoionization models of the CISM and in situ pickup ion data will directly constrain the local ISM composition for N, O, Ne, and Ar.

5.3.2. Requirement for supplementary source of hard radiation.
As shown by Vallerga (1998), however, the observed stellar radiation field is inadequate to provide the ionization of He in the CLIC. Another important point is that the stellar radiation field alone is also unable to provide heating necessary to maintain the CLIC at its observed temperature of ∼6,000–7,000 K. Dust heating alone is also inadequate to balance the cooling in the gas. Turbulence has been proposed as another heating source (Minter & Spangler 1996), but the small magnitude of the turbulent line widths makes this source doubtful. This leaves the diffuse interstellar radiation field as the most likely source of the heating in photoionization equilibrium models. Models predict that photoionization of HI, HeI, and photoelectric ejection of electrons from dust grains provides 66%, 25%, and 6% of the cloud heating, respectively (Slavin & Frisch 2008). Over 85% of the cooling is from forbidden lines. The radiation field is required to provide the inferred level of He ionization and enough heating in the cloud to maintain the thermal balance at the observed temperature of ∼6,000–7,000 K. We note that the partially ionized nature of the cloud in combination with its temperature cannot be attained even for a relatively hard stellar radiation field, e.g., a B1 star,

because the ionized regions produced by such an ionizing field will become cool before it becomes partially neutral. That is, as radiation propagates into the ISM, absorption leads to a drop in heating before the ionization level decreases, resulting in partially ionized gas at cooler temperatures than observed in the CLIC.

5.4. Models for the Local Interstellar Cloud–Intercloud Boundary

5.4.1. Evaporative boundaries. In the context of the radiative transfer models (Section 5.3), the required supplementary source of EUV radiation can be provided by a conductive interface between the LIC and Local Bubble hot plasma. The LIC is warm, $T \approx 7{,}000$ K, whereas the very low density surrounding the hot plasma is controlled by collisional ionization. The ionization in the boundary between these diverse regions is poorly constrained. If the very low-density ISM filling the Local Bubble interior is hot, the strong temperature gradient should drive heat flux into the cloud and cause an evaporative outflow. Any gas in the intermediate temperature range, $T \sim 10^5$ K, will radiate strongly in the EUV because of the existence of HeII, the abundant Li-like ions CIV, NV, and OVI and Na-like SiIV, which have strong resonance lines that are excited at these temperatures. Detailed models assume an interface as the boundary of a spherical cloud that evaporates via thermal conduction into the surrounding hot gas (Slavin 1989, Slavin & Frisch 2008). These models assume a steady outflow and include the effects of radiative cooling, saturation of thermal conduction (see Cowie & McKee 1977), and reduction of effective thermal conductivity by the magnetic field. In addition, the strong effects of nonequilibrium ionization in the boundary are taken into account. These effects are particularly strong in the evaporative outflow because the weakly ionized cloud material is heated on a timescale that is very short compared with its ionization timescale, leading to highly underionized gas at temperatures of 10^5–10^6 K. The EUV/soft X-ray emission from this gas provides a natural extra source of the hard ionizing photons needed to explain the high level of He ionization in the cloud.

5.4.2. High-ion diagnostics of evaporative cloud boundaries. The best observational constraint on cloud evaporation models comes from absorption line observations of the so-called high ions that should exist in the boundaries. These ions include CIV, NV, and especially OVI, all of which have low abundance in hot ($\sim 10^6$ K) gas and peak in concentration under collisional ionization equilibrium conditions at temperatures of $\sim 10^5$–$10^{5.3}$ K. The most recent assessment of the data from FUSE observations of nearby stars (Barstow et al. 2010) finds that the OVI absorption is patchy. They find few detections of OVI within the Local Bubble. Most of the detections are for stars that are close to or just beyond the neutral boundary of the Local Bubble, supporting the existence of hot gas within the bubble but not lending support for evaporative boundaries on the clouds within the bubble. Welsh et al. (2010b) have recently reported the observation of narrow ($b = 6.8$ km s^{-1}) CIV absorption lines within the Local Bubble; one of the absorption lines was identified with the LIC velocity. In contrast, the evaporating cloud models predict large line widths; the ions persist into the hot gas because of the lag in ionization in the outflow. These broad line widths hamper attempts to observe the absorption lines because continuum placement becomes difficult and the peak absorption optical depth is less than that for narrower lines of the same column density. The cloud evaporation models also predict substantial outflow velocities for the gas, resulting in a velocity displacement relative to the neutral gas in the cloud. This could result in confusion when trying to separate photospheric absorption lines from interstellar lines. As an example, the cloud evaporation model 26 of Slavin & Frisch (2008), which uses a Local Bubble temperature of $10^{5.9}$ K, predicts a b value of 25 km s^{-1} for the OVI lines, an offset of 7.4 km s^{-1} from

the cloud velocity and peak depth of absorption of 3.6%. The same model predicts a CIV column of 2.9×10^{12} cm^{-2} with a width (b value) of 20 km s^{-1} (a factor of three larger than observed).

5.4.3. Evaporative boundary versus turbulent mixing layer. The lack of observational confirmation of the nature of the boundary between clouds in the CLIC and the surrounding hot gas creates a major unknown in the understanding of the equilibrium condition of the CLIC. To date, there has yet to be a clear-cut observation of an evaporative boundary on an interstellar cloud. There are a variety of reasons why that might be the case, ranging from the inherent difficulty of such observations, as discussed above, to cloud morphology and the physics of cloud evaporation. Electron thermal conduction is severely reduced perpendicular to magnetic field lines, and it has been proposed that the tangled magnetic fields that may exist in interstellar clouds, and especially at their boundaries, could prevent evaporation in most circumstances. Another possibility, proposed by Balbus (1985), is that a collection of clouds, such as the CLIC, have the effect of reducing the evaporation rate per cloud because of how thermal conduction alters the temperature in the hot medium between the clouds.

An alternative possibility is that there is shear flow of the hot gas past the warm clouds, which has led to turbulence and mixing of hot and warm gas in the boundary (Slavin, Shull & Begelman 1993). One piece of observational evidence that stands out as particularly relevant in this regard is the significant column density of SiIII observed along some lines of sight for the CLIC (e.g., Gry & Jenkins 2001). This ion should not exist in significant abundance in partially ionized gas because of the large cross section it has for charge exchange recombination with neutral H. Even the nonequilibrium ionization conditions present in an evaporating cloud boundary do not lead to SiIII column densities close to those observed. One possible explanation for the observed column densities is circumstellar gas, though the close match of velocity components with lower ionization gas makes this unlikely. In addition, on some lines of sight, there are several velocity components for the SiIII absorption, indicating that the lines originate in different clouds along the line of sight. One collisional ionization model that does produce substantial SiIII is the turbulent mixing layer models of Slavin, Shull & Begelman (1993). This occurs in these models because the gas in the mixing layer has a mixture of ionization from previously warm gas that has low ionization and previously hot gas that has high ionization. After the gas mixes it begins to cool, leading to eventual recombination in the mixed gas. There are a range of assumptions in these models, for example, steady mixing, that may not hold in reality. Newer hydrodynamical (Kwak & Shelton 2010) and magnetohydrodynamical models (Esquivel et al. 2006) have not examined this ion and, in any case, have not included all of the nonequilibrium ionization effects (e.g., nonequilibrium cooling). A critical test of these models will be the properties predicted for the SiIII line. Currently, there are no published models that correctly predict the SiIII column densities.

6. LOCAL GAS AND DUST COMPOSITION

In warm, partially ionized interstellar medium such as the CLIC, ionization corrections are needed for accurate gas-phase abundances and elemental depletions. Comparison of these abundances with solar abundances, shown by pickup ion isotope ratios to be a reasonable template for the local ISM composition (Section 3.2), allows the calculation of the number of atoms that must be depleted onto dust grains. We do not expect the gas-phase abundances or depletions to vary significantly within a single cloud if the cloud has a common history, although depletions do vary significantly in the LIC. Depletions and abundances in the general ISM are reviewed by Savage & Sembach (1996). Estimates of ionization levels in the CLIC (**Table 1**), based on radiative transfer models that correct for ionization variations, are a significant improvement over the line-of-sight models.
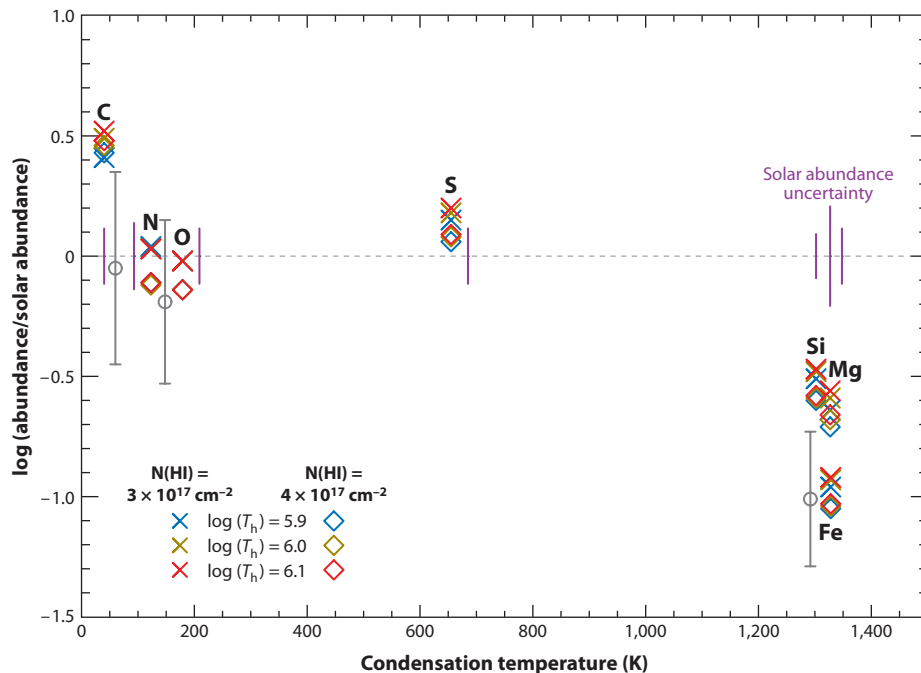
Figure 8

Interstellar elemental abundances relative to solar abundances versus condensation temperature for the element, as predicted by photoionization models of the local interstellar cloud. The symbol shape indicates the assumed H I column density towards ϵ CMa in the model, and the color gives the temperature assumed for the hot Local Bubble plasma. Elemental abundances in the models are determined by matching observed column densities for ions in conjunction with the predicted ionization corrections. The dark gray data points with error bars are derived from the C, N, and Si column densities for the Capella line of sight of Wood et al. (2002). Vertical purple lines indicate the quoted uncertainty in the solar abundance value (Asplund, Grevesse & Sauval 2005).

6.1. Elemental Depletions

Refractory elements in the ISM are progressively less depleted for clouds in the cold disk, warm disk, disk+halo, and halo. The abundance pattern of refractory elements in the CLIC, such as Mg, Fe, and Si, is comparable to warm cloud abundances. The ionization corrections in models of the CISM give typical depletions of $\delta(\text{Si}) \sim -0.50$ dex, $\delta(\text{Mg}) \sim -0.65$ dex, and $\delta(\text{Fe}) \sim -1.00$ dex (see **Figure 8**, where depletions from the gas phase are negative to indicate a deficit of an element). The depletion of an element, $\delta(X)$, indicates the quantity missing from the observable gas phase, $\delta(X) = \log(X_{\text{ISM}}/H_{\text{ISM}}) - \log(X_{\odot}/H_{\odot})$, where X and H are the gas-phase abundances for X element and H, respectively, in the ISM or abundances in the Sun ($\odot$). The Si and Mg depletions in the CISM are within 0.1 dex of galactic warm gas depletion patterns (table 5 of Welty et al. 1999), but Fe is less depleted by 0.4 dex than for general warm galactic gas.

Depletions of elements into dust grains in interstellar gas display a dependence on the condensation temperature of the element, which is the temperature at which 50% of the element has condensed out of the gas phase. In protostellar environments, minerals with high condensation temperatures, 1,500–1,800 K, such as Ca-, Al-, and Ti-rich oxide phases, condense out first; metal alloys, Ca-pyroxene, and nearly pure Mg-olivine condense out at below 1,450 K (Ebel 2000). Elements with the highest condensation temperatures are also the most depleted in the ISM, and

the gas-phase abundances of refractory elements are systematically higher in warm rather than in cold clouds (Savage & Sembach 1996, Welty et al. 1999).

6.2. Grain Composition

The composition of grains can be found for the CISM to higher accuracy than other warm clouds, where the ionization corrections are more uncertain. Using the LIC component in the ϵ CMa line of sight only (because of the completeness and high quality of the dataset), Slavin & Frisch (2008, Section 5.3) found substantial depletion of the elements that form silicate dust, namely O, Mg, Si, and Fe. Using the solar reference abundances (e.g., Asplund et al. 2009), these researchers found depletions of 15–35%, 80–82%, 72–77%, and 90–92% for those four elements, respectively, for the best models (models 26 and 27). Abundances in the LIC for Mg, Si, and Fe, after ionization corrections, are between warm and halo cloud abundances (see table 5 in Welty et al. 1999).

6.2.1. Silicates. Using protosolar abundances (Asplund et al. 2009) and the standard assumption that the elements missing from the gas are in the grains, the dust composition is found by subtracting the observed Mg, Fe, and Si abundances in the gas from solar abundances. Applying this process to the LIC densities, corrected for ionization, gives grains with $(Mg+Fe)/Si = 2.6 \pm 0.1$ for CISM models 26 and 27 (Section 5.3; see also Slavin & Frisch 2008). This composition suggests that the CISM grains contain olivine where $(Mg+Fe)/Si \sim 2$, rather than pyroxene where this ratio is ~ 1, and additional metals (Savage & Sembach 1996). If the gas-phase composition is characteristic of the destroyed grain mantles, the CISM models would indicate mantle material with $(Mg+Fe)/Si \sim 1.0$, which is characteristic of pyroxene. The relative Mg and Fe abundances in other clouds in the CLIC are also consistent with olivine grains, as shown in **Figure 9**.

6.2.2. Carbon. The overabundance of C in the CISM gas suggests that the carbonaceous grains are destroyed, although this is more controversial than the abundance of the silicate grain constituents. The uncertainties are due in part to the difficulties involved in interpreting the saturated absorption lines of CII. The most easily observed line, 1,334.5 Å, is a strong resonance line and is strongly saturated even for low column density lines of sight. For most lines of sight, the equivalent width of the line puts it on the flat part of the curve of growth, which results in very uncertain column densities. The CII* line, however, is much weaker and gives C abundances only if the electron density is known. The Slavin & Frisch (2008) models for the photoionization of the LIC, based on data for the ϵ CMa line of sight, indicate a C abundance ranging from 590 to 960 ppm. Relying only on estimates of the FUV background, and the CII*, MgI, and MgII observations, Slavin & Frisch (2008) derived a range of 400–800 ppm with a lower limit of 330 ppm. In either case, when compared to the solar C abundance of 295 ppm, C appears to be overabundant in the gas phase.

Another high-quality data set is that of Capella, which shows a single absorption line at a velocity consistent with the LIC velocity (Wood et al. 2002). An overabundance of C in the gas phase is not found toward Capella, where cloud ionization is also determined. Because Capella has a LIC column density $N(\text{HI})$ an order of magnitude larger than found toward ϵ CMa, and because the LIC depletions between Capella and Sirius differ by ~ 0.5 dex, quite possibly both the gas and dust differ in the LIC component for these two directions. However, data on the first three ionization stages of C, N, and Si toward Capella fully account for possible ionization variations, and the ionization levels for these three elements match the predictions by Slavin & Frisch (2002). Wood et al. find depletion levels of $\sim 11\%$, $\sim 29\%$, and $\sim 91\%$, for C, N, and Si, respectively.
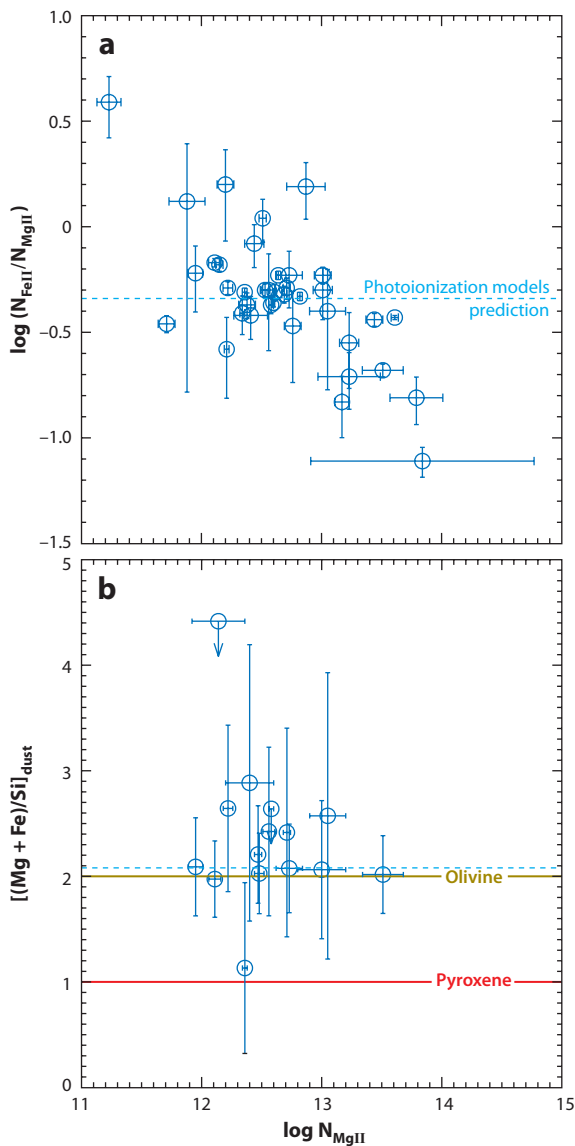
Figure 9

(*a*) The ratio FeII/MgII is compared to MgII abundances in the cluster of local interstellar clouds (CLIC).
The dashed light blue line shows the prediction for this ratio from photoionization models, which also
predict that 15% of Mg is doubly ionized (Slavin & Frisch 2002). (*b*) Ratios of refractory elements in CLIC
dust grains for selected sightlines with adequate data. The ratios are obtained by comparing the gas-phase
abundances of the elements with protosolar abundances that describe the complete interstellar abundances
for each element (see Section 6). The ratio (Mg+Fe)/Si distinguishes between olivine minerals (∼2) (*dark
yellow line*) and pyroxene silicates (∼1) (*red line*). Olivine silicates are the preferred grain composition
according to these data.

6.3. Variations in MgII versus FeII

Given the large-scale variations in galactic depletions between warm and cold ISM, it is a surprise to find that the relative gas-phase abundances of MgII and FeII vary over the nearest 10 pc and inside of individual clouds (Redfield & Linsky 2008). **Figure 9** shows that the ratio N(FeII)/N(MgII) anticorrelates with N(MgII) in the CLIC. Because both FeII and MgII are dominant ionization states in the CISM (with FeIII ~2.4% and MgIII ~15%; see **Table 1**), the relative variations in Fe and Mg gas-phase abundances represent true variations from cloud to cloud in the CLIC.

Several different studies have shown that Fe and Mg abundances are higher in the upwind direction than the downwind direction. Redfield & Linsky (2008, their figure 23) plot Mg and Fe depletions for components in the LIC and G cloud and reach a similar conclusion as the earlier studies.

Figure 7 of Frisch et al. (1999) shows that the observed abundances of Mg, Si, and Fe in the local ISM are consistent with the destruction of silicate dust grains through sputtering in supernova shocks of velocity ~100 km s^{-1}. If the CLIC is assumed to have originated as a colder cloud complex, some processing of the CLIC dust grains through shocks is required to produce the observed warm cloud abundance patterns. The analysis of the 15 kinematical objects in the CLIC of Redfield & Linsky (2008; and see Section 4) shows that the weighted mean turbulence correlates with weighted mean depletions in the clouds, which are attributed to grain destruction in turbulent regions where clouds interact. The researchers speculate this occurs because high turbulence regions are created by the dynamical interactions of clouds that produce shocks that destroy the dust. However, the present turbulent velocities are quite low, ~1–3 km s^{-1}, far below the speeds at which significant grain destruction is likely to occur. Thus, if this correlation is to be explained as caused by grain destruction, it must have roots in the cloud history with the turbulence related to the speed of shocks that passed through the cloud sometime in the past. The depletions are generally calculated with respect to HI (or DI). Inclusion of the ~50% ionized gas toward the NGP component in η UMa (Section 5; see also Frisch et al. 2011, in preparation) decreases depletions by only ~0.3 dex and strengthens the correlation.

6.4. Gas-to-Dust Mass Ratio

The gas-to-dust mass ratio, $R_{g/d}$, can be found in two independent ways for the CISM. The in situ *Ulysses*, *Galileo*, and *Cassini* measurements of the interstellar dust-mass distribution in the heliosphere (Frisch et al. 1999, Mann 2009) give $R_{g/d} = 116$ and 123 for models 26 and 27, respectively (table 9 in Slavin & Frisch 2008, where the model dependence arises in the prediction for the total gas density). Using instead the derived depletions based on assumed reference abundances to get the dust mass, the same models, 26 and 27, predict gas-to-dust ratios of $R_{g/d} = 217$ and 321, respectively (using the abundances of Grevesse, Asplund & Sauval 2007, other solar abundance sets imply somewhat lower values for $R_{g/d}$). The factor of two discrepancy between $R_{g/d}$ from the radiative transfer models versus in situ measurements is a puzzle, because it appears to indicate decoupling of dust and gas over parsec scales (e.g., see references in Mann 2009).

However $R_{g/d}$ correlates with the percentage of dust mass carried by Fe (in other words, depletion of Fe stays relatively constant as depletions of the other elements vary) when both cold and warm clouds are included in the sample (figure 2 of Frisch & Slavin 2003). This characteristic may explain both the difference between the in situ and LIC $R_{g/d}$ values and the correlation between FeII/MgII and MgII. High $R_{g/d}$ values indicate grain destruction in interstellar shocks, which may leave behind resilient iron-rich cores (Savage & Sembach 1996). Wood, Linsky & Zank (2000) and Redfield & Linsky (2008) find that MgII abundances are a factor of ~4 higher in the

G cloud than the LIC. Frisch (2010) finds that sightlines with galactic longitude larger than 180°
show systematically larger FeII column densities at a given distance, for stars within 60 pc, than
sightlines with longitudes less than 180°, without a similar effect for DI. Either the variations in
grain destruction occurred between clouds in the CLIC, or grains and gas have become decoupled
in some local regions, or higher cloud ionizations are prevalent nearby for $\ell > 180°$.

7. INTERSTELLAR MAGNETIC FIELD

For partially ionized diffuse ISM such as the CLIC, the interstellar magnetic field is an essential
ingredient for understanding the equilibrium, dynamics, and history of the gas. The effect of Loop
I on the kinematics of the local clouds is quite obvious, but it is an open question as to whether
Loop I dominates the properties of the magnetic field at the Sun.

7.1. Direction and Strength of Local Interstellar Magnetic Field

The direction of the interstellar magnetic field in the Solar Neighborhood has now been measured
roughly over five orders of magnitude in scale sizes, including the ∼90-pc radius of the radio Loop
I, optical polarization data giving the magnetic field direction within 5 pc, and at scales of ∼150 AU
where the IBEX Ribbon is formed. The center of the IBEX Ribbon arc, ℓ, b = 33°, 55° gives
the interstellar magnetic field direction at the solar location (Section 3.2.4). Disparate diagnostics
of the direction of the interstellar magnetic field near the Sun such as the radio pulsar, optical
polarization, radio continuum polarizations, and the IBEX Ribbon, all provide similar directions
to within ∼ ±35° (see below). This similarity suggests that the overall local field is smooth, but
more detailed discussions of magnetic turbulence await additional data.

No direct measurements of the magnetic field strength in the LIC are available. From the
assumption of equipartition between magnetic and thermal pressure in the LIC, one obtains a
strength of ∼2.7 μG for the magnetic field in the CISM (Slavin & Frisch 2008). MHD heliosphere
models designed to reproduce the IBEX and other heliosphere data also provide the most likely
source of accurate information on the strength of the interstellar magnetic field at the Sun, but
uncertainties are still large, 2.7–5 μG (Section 3.3).

7.1.1. Local magnetic field from pulsar dispersion and rotation measures. The direction
and strength of the global magnetic field in our neighborhood can be found from pulsar data
that measure both the dispersion of the pulse packet due to wavelength-dependent refraction
in the interstellar plasma and the Faraday rotation of polarization that occurs where the parallel
component of the interstellar magnetic field traverses a plasma. Thus, comparisons between pulsar
dispersion measures and rotation measures provide the parallel component of the large-scale
magnetic field strength and polarity within kiloparsecs of the Sun (e.g., Han 2006). Unfortunately
no pulsars are available to sample the magnetic field within 50 pc of the Sun. In the low-density
Local Bubble interior of the third galactic quadrant, $\ell = 180°-270°$, the magnetic field strength
and direction are derived from four pulsars that are 150–300 pc away (Salvati 2010). Salvati found
a magnetic field that is directed toward ℓ, b = 5°, 42°, with a strength of ∼3.3 μG.

7.1.2. Local magnetic field direction from radio continuum shells. The direction of the
interstellar magnetic field found over scales of ∼80 pc by Wolleben (2007) for the S1 shell of
Loop I (Section 2.3) is toward ℓ, b = 71° ± 30°, 18° ± 30°. This direction is within 30° of
the magnetic field directions from the optical polarization. The S1 shell direction is based on

high-latitude radio continuum enhancements of polarized 1.3-GHz emission, and this agreement may be coincidental if the shell is not spherical.

7.1.3. Magnetic field direction from optical polarization. Optical polarization can be a sensitive diagnostic for the magnetic field. Starlight is polarized when starlight traverses a birefringent medium created by magnetically aligned interstellar dust grains, with possible additional polarization from regions of very intense radiation (Lazarian 2007, Draine 2009). Interstellar polarizations are parallel to the magnetic field direction because the ISM opacity created by magnetically aligned interstellar dust grains is lower in directions parallel to the magnetic field than in perpendicular directions, providing that radiative alignment is insignificant.

For distant stars, the maximum observed polarizations are approximately proportional to dust extinction and are only 40% of the possible theoretical polarization due to foreground depolarization (Fosalba et al. 2002). For extended sightlines, the relation $P_\% \leq 3.5E(B-V)^{0.8}$ links polarization and color excess. After incorporating *Copernicus* data for intercloud stars, giving $N(H)/E(B-V) = 5.0 \times 10^{21}$ cm^{-2} mag^{-1} for hydrogen column densities $N(H)$ (Savage & Bohlin 1979), global polarizations are characterized by $P_\% \leq 1.53 \times 10^{-17} N(H)^{0.8}$.

Nearby stars inside of the Local Bubble cavity have a deficit of polarization per unit distance when compared to distant stars (PlanetPol data; see Bailey, Lucas & Hough 2010); however, the polarization per unit column density appears higher for some stars. Toward 36 Oph (5 pc) $N(HI) = 10^{17.82}$ cm^{-2}, giving a predicted polarization of 0.0028% for the limits set by reddened stars. Comparing this prediction with the larger observed value of 0.018% $\pm$ 0.007% (1σ uncertainties; see Tinbergen 1982) suggests there has been minimal disruption of grain alignment by collisions and that a single polarizing screen is within 5 pc of the Sun in this direction.

Tinbergen (1982) detected a patch of very weak interstellar polarization, ~0.02%, near the Sun in the fourth galactic quadrant and at negative ecliptic latitudes (Frisch 2005). The location of the patch coincides with the G cloud (Section 3). The closest polarized star is 36 Oph, which is 10° from the heliosphere nose (Section 3.2). The high-sensitivity PlanetPol polarizations show a weak dependence on distance for stars within 30 pc, but this dependence is barely apparent in the lower sensitivity Tinbergen data.

Five of the Tinbergen stars form a polarization peak toward the heliosphere nose, which is defined by a consistent polarization position angle. This grouped polarization allows the possibility that interstellar dust interacting with the heliosphere may contribute to the polarizations (Frisch 2005). Interstellar dust grains with radii ~0.01 μm form a dust wall around the heliosphere nose and outside of the heliopause (Slavin et al. 2010). At distances of ~250 AU, where the 0.01-μm grains are deflected around the heliosphere toward the nose direction, the grain charge is ~1 V (Z ~50) and the grain gyroradii are less than 1 AU (Slavin et al., in preparation; Mann 2009). Contributions to the polarization from the outer heliosheath regions are possible, although yet unproven.

The direction for the magnetic field close to the Sun has been found from the polarizations of nearby stars. The position angle of the polarization vector, *PA*, is the angle between the polarization vector and the north-south meridian. Frisch et al. (2010a) determined the direction of the local interstellar magnetic field that is most consistent with polarization data for ~30 stars within 40 pc of the Sun and within 90° of the heliosphere nose for the assumption that the field is a dipole. The best-fitting field was determined by minimizing the function $F = \overline{\sin(PA_j)_i}$ for j stars, evaluated over i possible magnetic field directions on the sky. The broad minimum in F gives a magnetic field direction that is directed toward $\ell, b = 38°, 23°$, with uncertainties of $\pm 35°$. This magnetic field direction is close to the ISMF direction obtained from the IBEX Ribbon. **Figure 10** shows the polarization vectors used to determine the best-fitting ISMF. The
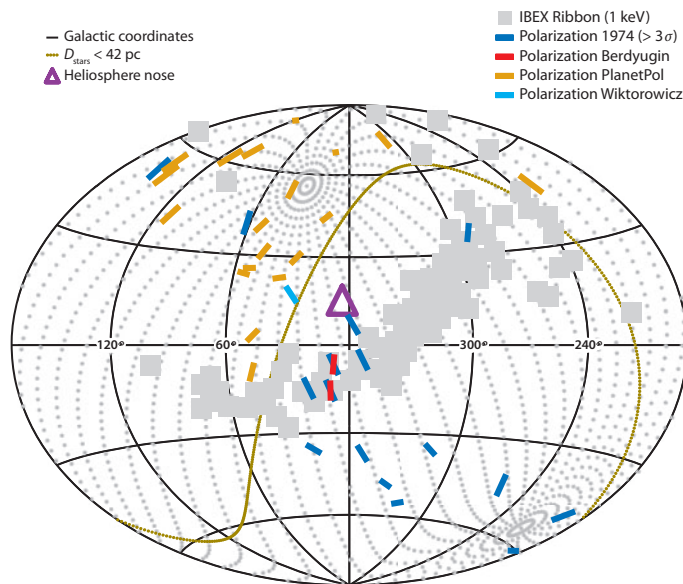
Figure 10

The gray grid of points shows the direction of the interstellar magnetic field at the heliosphere that is indicated by the center of the IBEX Ribbon arc, which is toward L, B = 33°, 55°. The highest flux regions of the IBEX Ribbon in IBEX-HI data at 1 keV are shown as the filled gray region. The fluxes correspond to values larger than ~1.5 of the mean. The short colored bars show the directions of the polarization vectors used to obtain the best-fitting local ISMF direction of L, B ≈ 38°, 23°

magnetic field direction obtained from the position angle data agrees, to within uncertainties, with the magnetic field direction derived from the center of the Ribbon arc. The strongest regions of the IBEX Ribbon, for IBEX-HI 1 keV data (McComas et al. 2009a), are also plotted in **Figure 10**. The group of polarizing stars near the heliosphere nose overlay the Ribbon direction.

7.2. Is Magnetic Pressure Important for the Cluster of Local Interstellar Clouds?

Although magnetic fields and turbulence govern the evolution of the supernovae-driven ISM on the large scale, magnetic pressure is generally ignored on the small scale for cloud pressure calculations. Magnetic fields should play a role in the dynamical equilibrium of the CLIC because of the influence of Loop I on the CLIC dynamics. For warm, very diffuse ISM such as the CLIC, an important aspect of pressure equilibrium is whether high ratios of thermal to magnetic pressures, $\beta_P = P_{thm}/P_{mag}$, influence the evolution and stability of clouds. This can be guesstimated for local clouds. If we assume a local magnetic field strength of ~3 μG and typical total cloud densities similar to the LIC of 0.33 cm^{-3} (including neutrals and ions), then the temperatures of the 15 clouds listed in table 8 of Redfield & Linsky (2008) give $\beta_P = 0.4$–1.5. This range suggests, but does not prove, that the magnetic field is important in CLIC stability. Current data are inadequate to further constrain β_P.

Observations of the Zeeman splitting of the HI 21-cm hyperfine line in cold clouds are a rich source of data on the parallel component of the magnetic field. Heiles & Troland (2005) find a median field strength of 6 μG for such clouds. Unfortunately, the CLIC column densities are much too small for such observations locally. If flux freezing holds for the local magnetic field

strength, then the local strength could be guessed from the ratio of the square of the densities in dense and tenuous ISM. However, flux freezing is seen only down to densities of $\sim$300 cm^{-3} (Crutcher et al. 2010). The Salvati (2010) pulsar results discussed above appear to be a more reliable indicator of the strength of the local magnetic field.

The strength of the very local magnetic field also determines whether the heliosphere has a bow shock, because at the CISM temperature of 6,300 K, ion density of 0.07 cm^{-3}, and relative Sun-cloud velocity of 26.3 km s^{-1}, a magnetic field strength of 3 μG would correspond to a bow shock Alfvénic Mach number of $M \sim 1$.

7.3. Strange Implications of Local Magnetic Field Direction

We would be remiss if we didn't mention one of the most peculiar coincidences relating to the local magnetic field direction. The direction obtained from the optical polarization data (**Figure 10**) mimics the symmetry of the dipole moment of the cosmic microwave background (Frisch et al. 2010a). The great circle in the sky that divides the hot and cold poles of the cosmic microwave background dipole moment traverses the heliosphere nose region as defined by the Witte (2004) HeI direction (Section 3.2). It is also roughly coincidental, to within $\sim$10°, with the best-fitting local magnetic field direction. Continuing study of the weak interstellar polarizations of nearby stars is needed to confirm the reality of this effect.

## 8. MORPHOLOGY OF INTERSTELLAR MEDIUM NEAR THE SUN

8.1. Warm Clouds

From the original efforts to connect nearby interstellar clouds with French cartoon characters (Lallement, Vidal-Madjar & Ferlet 1986) to the squall line of upstream ISM thrusting past the Sun into the downwind local fluff (Frisch 1995), much thought and effort has gone into extracting convincing information about interstellar structures from high-resolution spectral observations of nearby stars (e.g., Frisch 1994, Gry 1996, Redfield & Linsky 2000). Reconstruction of cloud structure depends on information about HI volume densities, which is known only for the CISM locally. The CI fine-structure lines that show a bimodal distribution of pressures in denser regions (Jenkins & Tripp 2007) are too weak for detection in the CLIC. Ionization also plays a key role in the visibility of a cloud in absorption lines, especially for trace ionization states such as CaII that contains only $\sim$2% of the available gas-phase Ca (**Table 1**).

A 3D morphological model of the local ISM, independent of a formation mechanism, can be developed using observed column densities, together with an assumption of homogeneous interstellar densities in the local volume of space. Redfield & Linsky (2000) presented such a model for the LIC. The results indicate that the LIC can be modeled as a quasi-spheroid with the Sun near the LIC boundary. A reanalysis of the LIC morphology with an expanded data set of 57 sight lines is presented by S. Redfield & J. Linsky (in preparation), which confirmed the shape of the earlier model made with only 16 lines of sight (see **Figure 11**). The diameter of the LIC is $\sim$2.5 pc, and its mass is $\sim$0.32 M$_\odot$.

Modeling the morphology of the other clouds in the immediate vicinity of the Sun and the LIC has the complication that in addition to the cloud path length (based on the observed column density), an estimate is needed for the distance of the cloud itself. S. Redfield & J. Linsky (in preparation) present a morphological model of the CLIC that uses the distances of observed stars to constrain the location of local clouds. **Figure 11** shows the results of this model as viewed from the North Galactic Pole. Several notable characteristics of the local ISM morphology are
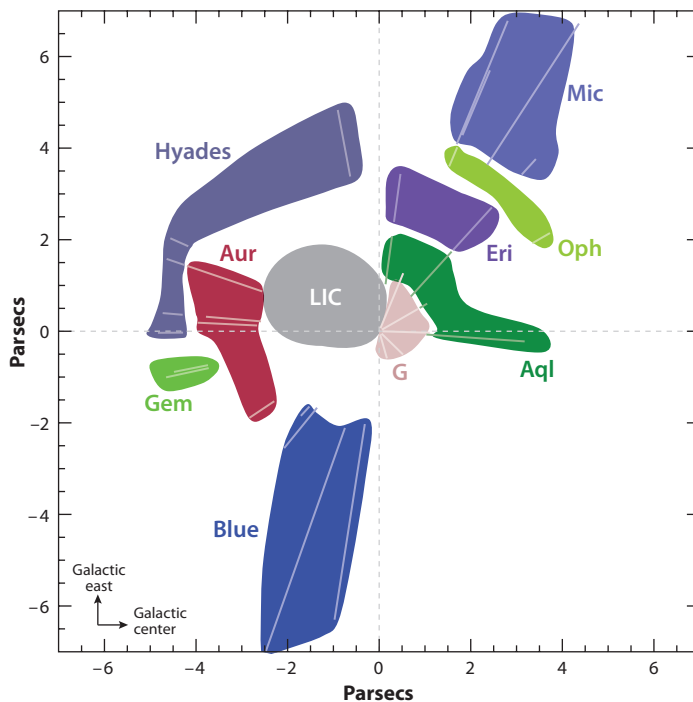
Figure 11

The location of interstellar clouds in the Galactic Plane, as viewed from the North Galactic Pole, that are close to the heliosphere from the set displayed in **Figure 5**. The local interstellar cloud (LIC) and Blue Cloud are seen in front of Sirius (2.6 pc). The Haud region of cold clouds is seen near the intersection of the Gem and Aur clouds and has a similar bulk motion as the Gem cloud (Figure from S. Redfield & J. Linsky, in preparation). Some of the clouds are named after the constellations toward which they are observed, e.g., Oph, Leo, Cet, Vel, Aql, Eri, Mic, Aur, Dor, and Gem. The other clouds are the LIC, the G-cloud in the Galactic center hemisphere, the North Galactic Pole (NGP) cloud, and the Blue cloud. Hyades denotes the stellar cluster containing many of the stars that sample that cloud.

that the LIC is in the middle of the complex of local clouds; some clouds show filamentary or elongated structure, whereas others are spherical, but the clouds at the leading edge of the CLIC (i.e., the Hyades and Aur clouds) drape around the LIC, whereas the distribution of the other clouds themselves lie along an axis at roughly $\ell \sim 60°$ and $\ell \sim 240°$. A uniform density is assumed to derive the thickness of the clouds, and the angular extent is given by the sightlines where the kinematical components are observed.

The 3D morphology of the CLIC will provide an important constraint on the theories of the origin of these clouds (see Section 9). Also, a model of the spatial distribution of clouds, together with ionizing sources in our local environment, would make it possible to model the ionization structure of the CLIC. Currently, as discussed in Section 5, we are primarily limited to modeling the ionization structure of the CISM, but a 3D morphological model of the CLIC would enable a direct comparison with an ionization model and line-of-sight observations of ions toward nearby stars.

Another approach is to utilize a plausible association of the CLIC with a Loop I subshell that has an embedded magnetic field [e.g., the Wolleben (2007) model; see **Figure 6**; see also Frisch & Müller 2011]. The upwind direction of the bulk LSR CLIC velocity is ~15° from the center of the S1 shell center at $\ell, b = 346° \pm 5°, 3° \pm 5°$ (**Table 2**). The best fitting magnetic field for

the CLIC makes an angle of $\sim70° \pm 35°$ with the LSR CLIC velocity, suggesting that the cloud velocities are flowing roughly perpendicular to the magnetic field direction. Models of the spatial distribution of local FeII and CaII in terms of the Wolleben (2007) Loop I model, however, could not distinguish conclusively between a smooth distribution for these ions versus clumping in the rims of the S1 and S2 shells (Frisch 2010).

8.2. Tiny Cold Clouds

The tiny cold HI structure in Leo (Section 4.1) has a filamentary morphology for a distance of 20 pc, with dimensions of $\sim0.07 \times 0.6 \times 2.4$ pc. Haud (2010) estimates that the ring interacts with the S2 shell at a distance of ~33 pc from the Sun. Redfield & Linsky (2008) speculate that the cold clouds are produced by the compression of the slow Leo and Aur clouds by the relative 12 km-s^{-1} motion of the Gem cloud (**Figure 11**). The velocity vector of the Gem cloud in the LSR (using the conversion in **Table 2**) is within 10° and 1.0 km s^{-1} of the bulk velocity of the Haud ring, suggesting that the Gem cloud may be a segment of the Haud ring (although the distances of the two features disagree by >5 pc). Density peaks at the stagnation points of converging flows may account for tiny structures such as these clouds (Hennebelle & Audit 2007), although the large-scale, ring-like configuration suggests a possible origin ordered by a more distant source. Because the radio feature is rotating and expanding, an association with the region of merging clouds identified in Linsky, Rickett & Redfield (2008) suggests that cold neutral gas may also be found elsewhere in the 15-cloud complex, perhaps even producing hidden saturated features at the UV resolutions.

9. ORIGINS OF THE INTERSTELLAR MEDIUM CLOSE TO THE SUN

The kinematics of the nearest ISM suggest that the origins of local ISM is related to the evolutionary processes that shaped the Local Bubble cavity and its contents (Section 2.1). However, because the hot low-density gas plays a key role in the thermal properties and evolutionary characteristics of a cloud, it will be difficult to establish the origin of the CLIC before the SXRB is fully understood. Although a range of physical properties of the nearby warm clouds are well established and provide important constraints on any theory of origins, perhaps the most discerning property is the velocity structure of all the nearest clouds (Section 4). Below we review several theories for the origin of the nearby ISM.

9.1. Multiple Supernova and Corollary of Superbubble Shell

Giant superbubble shells are common features associated with stellar evolution, as winds from O-B stars and supernova shocks evacuate low-density bubbles in the ISM (de Geus 1992). The common velocity and concentrated location of the nearby clouds might be explained as a relatively narrow superbubble shell passing across the Solar Neighborhood. The Sco-Cen Association provides a possible energy source for such an expanding shell, with three epochs of star formation that formed the Upper Centaurus-Lupus, Lower Centaurus-Crux, and Upper Scorpius subgroups. Indeed, we can identify Loop I as a shell formed by supernovae in Sco-Cen. Frisch (1981) concluded that the kinematics of ISM inside and outside of the heliosphere were consistent with an asymmetric expansion of the Loop I shell into the low-density Solar Neighborhood, as were the enhanced abundances of refractory elements in the CLIC that indicated shocked grains. De Geus (1992) modeled the superbubble shells associated with the three subgroups of the Sco-Cen Association, keeping track of energy input from the winds of massive stars and clustered supernova. He found a distance and radius of the superbubble associated with the formation of the Upper Centaurus

Lupus subgroup are 140 ± 20 pc and 110 pc, respectively, which places the Sun in or near this shell. This model was elaborated on by Frisch (1995) using more realistic values for the preshock gas and allowing the 5-Myr lull to evaporate gas from residual molecular clouds in the bubble between formation of the Lower Centaurus-Crux and the most recent Upper Scorpius subgroups, so that the most recent supernova shock expanded through the evaporated gas. The radius, 155 pc, and velocity, ~22 km s^{-1}, predicted for this superbubble shell using models for superbubble formation (e.g., Mac Low & McCray 1988) are consistent with CLIC properties although both are sensitive to the properties of the preshock gas and energy injected by supernova.

Radio observations of the Loop I superbubble shell motivate a model of two spherical magnetic subshells that explain high-latitude polarized radio emission and that, when extrapolated, place the Sun in the S1 shell (Wolleben 2007). It is unclear whether the distribution of material in the CLIC and the local cavity (as illustrated by the NaI and CaII maps) is consistent with this scenario. Frisch (2010) explores this model in more detail and highlights the unresolved issues when using this model to describe the CLIC configuration, which are the assumptions of spherical symmetry and that ISM is uniformly distributed in the shell. Indeed, we know that the local environment is not uniform, particularly in the direction of Sco-Cen. Another issue, whether a significant amount of dense material at the interaction zone of the Local Bubble and Loop I would alter the evolution of such a shell, may be moot if the shell traversed this interaction zone before it refilled with ISM.

The superbubble shell model naturally explains the kinematics of the CLIC, which show an upwind direction toward the center of Loop I (Section 4), and the abundance pattern that is similar to shocked ISM (Section 6). It appears that the field close to the Sun is consistent with the magnetic field direction of the S1 shell (which has large uncertainties in direction; Frisch et al. 2010a).

The micron-sized interstellar dust grains found in the Solar System appear to be related to the micron-sized grains that create coreshine IR emission in molecular cloud cores (Section 3.2.2). This suggest that the supernova shock that created the shell at the Sun would have traversed ISM evaporated from molecular clouds. However, it is not clear if even the large grains would remain intact if driven by a shock from the Scorpius-Centaurus region to the present location. Slavin (2009) suggests, instead, that the large grains originate from a local molecular cloud impacted by a shock.

9.2. Instabilities from Interaction of Loop I and the Local Bubble

Breitschwerdt, Freyberg & Egger (2000) present a model that explains the local clouds as being formed from a Rayleigh-Taylor instability in the interaction zone between Loop I and the Local Bubble. A pressure imbalance forms from reheating of Loop I, destabilizing the compressed interaction between the two bubbles. Magnetic reconnection enhances the creation of blobs of ISM, which are ejected ballistically into the Local Bubble from the interaction zone. Supporting this model is that a screen of material, squeezed at the interaction zone, seems to be present in the NaI density maps of the region (Crutcher & Lien 1984, Lallement 2009) and in counts of EUV sources (Warwick et al. 1993). Egger & Aschenbach (1995) find interstellar gas at ~70 pc that formed in the interaction ring and that shadows the soft X-ray emission of Loop I behind the ring.

This model has some attractive features, because it naturally explains the common velocity vector of local clouds, the warm-cloud abundances of the CLIC that result from shocks in the interaction regions, and the small sizes of the blobs. It does not satisfactorily explain the filamentary and sheet-like structures seen in the CLIC (Section 8) or the accumulation of clouds in the immediate vicinity of the Sun. A spatially distributed set of clouds might be expected to make the journey from the interaction zone toward the center of the Local Bubble, which is not observed, and it is not clear if the ejected blobs would have similar kinematics. Although it is possible that the

Rayleigh-Taylor instability would operate for a short time during the initial interaction, the Sun would have to be now passing through ISM from that burst of blob formation. One interesting test would be the smoothness of the magnetic field in the CLIC, because the blob model would predict relatively random field directions if magnetic reconnection is a factor in blob creation.

Arguing against this model are the pronounced differences in the west and east portions of the interaction ring, in both the magnetic field direction and distance of the feature. These differences suggests that this interaction ring is instead the chance superposition of different features (Santos, Corradi & Reis 2010).

9.3. Magnetic Flux Tube

For a multiple supernova origin for the Local Bubble (Smith & Cox 2001), the magnetic structures that are pushed to the edges of the cavity by supernova shocks may be rebounding. Cox & Helenius (2003) explore this scenario as a possible explanation for the origins of the nearby ISM, using a flux tube that parted from the Local Bubble cavity walls ∼3 Myr ago. Local Bubble material is swept up and flows toward the center of the rebounding magnetic flux tube to produce a transient collection of warm, partially ionized clouds near the center of curvature. This model provides a mechanism for a common kinematic driver for the local clouds. Predictions of this model include a strong magnetic field (6–7 μG, for pressure equilibrium with a 10^6 K plasma) and patchy distribution of highly ionized species (e.g., OVI). Most of the resulting warm clouds are expected to be short-lived and either expanding or contracting. Although it also addresses the local collection of clouds, it seems unlikely that a maverick, isolated event would account for local structure. The dynamics of the LIC, for instance, do not show signs of contraction or expansion. Although there is evidence for warm absorbers throughout the Local Bubble, it appears that most of the warm gas in the Local Bubble is located very near the Sun. This model predicts the magnetic field configuration near the Sun as somewhat smooth, except for density cusps that form clouds, which is a testable prediction.

9.4. Unanswered Questions About the Cluster of Local Interstellar Clouds

9.4.1. What is a cloud?
The appearance of depletion variations within a single cloud (for instance by a factor of 10 in the LIC) are in conflict with the notion of a cloud as a kinematically identified object with common properties and a common history.

Models of superbubble evolution in a turbulent magnetized medium predict transient clouds out of equilibrium and created from ISM with different histories (Mac Low et al. 2005). The depletion variations could thus imply that the kinematically identified clouds close to the Sun are transient artifacts of turbulence in an inhomogeneous medium, where the turbulent spectrum creates clustered velocities of objects with different histories. However, the apparent coherent motion of the LIC through space (**Figure 3**) instead suggests the clouds are stable entities.

A separate explanation for these depletion variations is that the CLIC represents fossil ISM from a previous inhomogeneous state where denser regions of the cloud were spared dust destruction (Slavin 2009).

An alternative is that ionization variations are present, because depletions are typically calculated in comparison to neutral HI or DI. Adding HII to the interstellar column density used in depletion calculations increases the number of atoms missing from the gas and thereby decreases the depletion values, e.g., increases the number of depleted atoms. However, the known ionizations of the LIC and NGP cloud (Section 5) (Redfield & Linsky 2008) do not appear to significantly alter conclusions about the depletion variations seen in those clouds.

9.4.2. Why does the cluster of local interstellar clouds exist? There are still many issues related to the origin of CLIC that are not understood. For example, why does the CLIC exist? From a theorists view, the existence of the local clouds within the hot gas of the Local Bubble needs explaining because of the penchant for clouds immersed in hot plasma to evaporate. For the classical evaporation rate calculated by Cowie & McKee (1977), cloud lifetimes would be ~10^6 years (for a 1 $M_\odot$ cloud). Including the effects of cooling, saturation of thermal conduction, and reduction of the effective conductivity because of the magnetic field leads to rates that may be lower by factors of ~4–10 (Slavin & Frisch 2008). The problems with explaining some of the data on high ions, as discussed in Section 5, may be telling us that the boundary is of a different type, perhaps involving shear flow and turbulence.

A second question relates to the dynamics of the CLIC, because the bulk motion away from the Sco-Cen superbubble center is clearly suggestive of an origin within that bubble. How such clouds propagate through space, and broader questions of the late stages of superbubble evolution, when shells begins to fragment, may shed light on the origin of the CLIC.

A possible source of warm, partially ionized material is cold dense gas that has been evaporated or shocked, and subsequently expands to lower densities in the low-pressure environment of the Local Bubble (Frisch 1995, Slavin 2009). The Local Bubble boundary is a potential source of such cold dense material, and the Sco-Cen association and its resulting expanding shells provide a possible source of a shock front. More modeling on the evolution of these structures as they travel through the Local Bubble is needed to understand whether the observational constraints on morphology, density, and ionization are consistent with the late stages of superbubble evolution.

9.4.3. What evidence is there for ongoing shock activity? Grzedzielski & Lallement (1996) modeled the relative velocities of the upwind and downwind gases as manifestations of a quasi-perpendicular MHD shock that propagates from the LIC into the G cloud. A plasma beta of $\beta_P = 1.3 - 1.5$ is required to match the predictions of the Rankine-Hugoniot equation for preshock and postshock temperatures and velocities. Note that this model requires no empty space with low-density plasma between the LIC and G cloud. The model also requires the shock to be recent enough that radiative cooling of the postshock gas has not yet occurred. Such a model naturally explains the deceleration of the CLIC flow.

10. PLANETARY SYSTEMS AND THE LOCAL INTERSTELLAR MEDIUM

The relative motions of the ISM and stars lead to variable astrospheres. The CLIC kinematics generate variations in the heliosphere over short timescales, perhaps even over historical timescales. Frisch & Müller (2011) estimate that for constant density clouds of 0.2 cm^{-3}, the mean cloud crossing time is ~47,000 years over the past ~10^5 years. Heliosphere models developed for different sets of boundary conditions show that even minor variations in ionization and velocity lead to significant variations in the heliosphere, whereas dramatic variations sweep away most of the heliosphere (Müller et al. 2009). Variations in the interstellar boundary conditions of the heliosphere have been shown to dramatically affect the flux of galactic cosmic rays at 1 AU (see chapters in Frisch 2006). For instance, one set of models predicts that the 30 MeV galactic cosmic ray fluxes would be larger than present fluxes at 1 AU by factors of 23 or 3–6, should the Sun be immersed in a dense cloud or the Local Bubble, respectively (Müller et al. 2006).

The Sun-local ISM interaction is not unique, but is likely replicated in many stellar systems that are surrounded by tenuous ISM with sufficient pressure to confine the stellar wind into a bubble. Astrospheres sample the ISM pressure at the star and provide a remote diagnostic of the interstellar magnetic field (Frisch 1993). Observations of hydrogen compressed in the interface

between the stellar wind and the surrounding medium have been detected for more than a dozen objects (see review by Wood 2004). But given the asymmetric geometry of astrospheres and the clumpiness of the local ISM, it is difficult to determine the fraction of nearby stars that have solar-like astrospheres. Given the growing number of known exoplanets in the solar vicinity, assessing their local ISM characteristics and understanding the structure of their astrospheres will be important in evaluating how the incident cosmic ray flux and the strength of the weak solar-type winds of the host star effect habitability and long-term planetary atmosphere evolution (Wood et al. 2005, Frisch 2006). Practically a quarter of all known exoplanets are within 30 pc of the Sun. Indeed, of those most easily followed-up (i.e., V magnitude ≤ 6), 58% are within 30 pc; and of those among the most desirable to be followed-up on, such as those with Super-Earth's within the habitable zone (Vogt et al. 2010) (GJ581) and those with 3 or more planets, 100% of these systems are within 30 pc.

Astrospheres are sensitive barometers of interstellar kinematics because the ISM ram pressure varies as velocity squared. Two identical clouds with different velocities can produce dramatically different astrospheres. Local 3D cloud velocities vary between 14 km s^{-1} (Blue Cloud) and 60 km s^{-1} (Cet Cloud, Section 4.2), giving a factor of 18 difference in the ram pressures exerted by clouds on an astrosphere for otherwise equal cloud properties. Additional causes of variation in astrospheres result from the ionization gradients in the ISM due to the strong gradient in the flux of ionizing radiation across the Local Bubble interior (Section 5, Section 2.2).

SUMMARY POINTS

1. The dynamic flow of clouds past the Sun provides an opportunity to study very low-density ISM with both astronomical techniques and in situ data. One can evaluate small-scale variations in the ISM, study the relationship between gas and dust in low-density clouds, and constrain the past and future Galactic environment of the Sun.

2. The ISM flowing past the Sun is warm, 2,000–12,000 K, with low mean densities, ~0.1–0.3 cm^{-3}. The turbulent broadening of the absorption lines formed in this flow anticorrelates with cloud temperatures. The warm ISM within 15 pc is clumped, with a filling factor of 6–19%.

3. The interstellar cloud surrounding the heliosphere is partially ionized—helium is ~38% ionized, whereas hydrogen is ~24% ionized. The helium ionization level is typical for the WIM, but higher levels of hydrogen ionization are seen for several other local clouds, as well as for the global WIM.

4. The direction of the interstellar magnetic field close to the Sun is determined by two methods—the weakly polarized light of nearby stars and the ribbon of ENAs originating from the outer heliosphere. These two disparate methods give similar interstellar magnetic field directions to within $\pm 35°$. Multifluid-MHD models of the heliosphere offer the best possibility for obtaining the strength of the local magnetic field.

5. The kinematical features in the nearby ISM have been divided into 15 separate clouds with similar kinematics and cloud temperatures. Depletions vary significantly within several clouds. Evidently either different parts of the local ISM have different histories, ionization varies over the region, or grain destruction via shocks is an ongoing process. The grain composition, implied by gas-phase abundances, suggests grains composed of olivine silicates.

6. One region where merging clouds are likely coincides with a region with tiny, dense, cold interstellar clouds, and that region is in Leo. The clouds are seen in NaI and HI and are within 25 pc. The cold gas is in a partial ring that shares the kinematics of the local ISM flow and slightly overlaps the positions of the S1 and S2 shells of Loop I.

7. Photoionization models of the interstellar cloud surrounding the Sun reconstruct the ionization levels for the interstellar gas that sets the heliosphere boundary conditions. Observations of interstellar neutrals inside of the heliosphere, such as HeI, provide a unique diagnostic of ISM ionization at the solar location.

FUTURE ISSUES

1. The nature of the very low-density ISM that provides the confining pressure for the local ISM clumps is uncertain. The soft X-ray emission from the hot plasma, originally thought to fill the Local Bubble, is contaminated by foreground emission from the heliosphere for energies above 0.2 keV. What is the nature of this very low-density ISM? There seems to be no alternative to the gas being hot, $T > 10^{5.5}$ K, because lower temperature gas would either cool too quickly or produce too much absorption or emission.

2. A persistent question relates to the source of the ionizing radiation for the nearby clouds. Some source of EUV or soft X-ray flux is required to explain the levels of helium, neon, and argon ionization. The ionizing radiation field depends crucially on the nature of the boundary between the warm and hot gas. The ArI data argue for the dominance of photoionization over nonequilibrium ionization effects.

3. The clumpy flow of ISM past the Sun indicates short-term variations in the properties of the ISM setting the heliosphere boundary conditions. The pickup ions and anomalous cosmic rays in the heliosphere would vanish if the Sun is in a fully ionized region. Maps of ionization variations in the CLIC will shed light on the source of historical variations in the Galactic cosmic ray flux on Earth.

4. The dynamics of the CLIC, moving directly away from the Sco-Cen superbubble center, is clearly suggestive of an origin related to that bubble. How such clouds propagate through space, and broader questions about the late stages of superbubble evolution when shells fragment, may shed light on the origin of the CLIC.

5. Do interstellar dust grains in the CLIC differ from grains in other low-density regions? In situ observations of very large grains in the Solar System are inconsistent with the ISM extinction data, but they are consistent with micron-sized grains seen in molecular cloud cores. In situ measurements of these large grains and their composition would help identify whether the local dust includes some molecular cloud ISM.

6. Measurements that would help resolve uncertainties relating to the properties of the boundaries between the local clouds and low-density plasma include: (*a*) measurements of highly ionized gases formed in cloud interfaces, including SiIV, CIV, and SiIII; and (*b*) improved atomic data for charge exchange emission for energies below 0.2 keV, where models of the SWCX are inconclusive.

7. A full survey of the ISM close to the Sun is needed to tie the present state of the CLIC to the dynamical origin and history of the local ISM. Such data would allow construction of a 3D model of nearby ISM and allow evaluation of the past and future of the heliosphere boundary conditions and the interplanetary environments of exoplanetary systems.

8. There is still an element of art involved in analyzing blended absorption lines, particularly in the UV where spectral resolutions are lower and the most important transitions are located. A dedicated spacecraft to obtain high-resolution UV data would allow detailed 3D maps of local ISM, leading to substantial advances in our understanding of the Galactic environment of the Earth and exoplanets.

DISCLOSURE STATEMENT

ACKNOWLEDGMENTS

LITERATURE CITED

Asplund M, Grevesse N, Sauval AJ. 2005. *ASP Conf. Ser.* 336:25–38
Asplund M, Grevesse N, Sauval AJ, Scott P. 2009. *Annu. Rev. Astron. Astrophys.* 47:481–522
Bailey J, Lucas PW, Hough JH. 2010. *MNRAS* 405:2570–78
Balbus SA. 1985. *Ap. J.* 291:518–22
Barstow MA, Boyce DD, Welsh BY, Lallement R, Barstow JK, et al. 2010. *Ap. J.* 723:1762–86
Begum A, Stanimirovic S, Goss WM, Heiles C, Pavkovich AS, Hennebelle P. 2010. *Ap. J.* 725:1779–85
Berdyugin A, Piirola V, Teerikorpi P. 2004. *Astron. Astrophys.* 424:873–76
Bloch JJ, Priedhorsky WC, Smith BW. 1990. In *IAU Colloq. 115: High Resolution X-ray Spectroscopy of Cosmic Plasmas*, ed. P Gorenstein, M Zombeck, pp. 160–63. Cambridge, UK: Cambridge Univ. Press
Bochkarev NG. 1987. *Ap. Space Sci.* 138:229–302
Bohlin RC, Savage BD, Drake JF. 1978. *Ap. J.* 224:132–42
Breitschwerdt D, Freyberg MJ, Egger R. 2000. *Astron. Astrophys.* 361:303–20
Bzowski M. 1988. *Acta Astron.* 38:443–53
Cowie LL, McKee CF. 1977. *Ap. J.* 211:135
Cox DP, Helenius L. 2003. *Ap. J.* 583:205–28
Cox DP, Reynolds RJ. 1987. *Annu. Rev. Astron. Astrophys.* 25:303–44
Crutcher RM. 1982. *Ap. J.* 254:82–87
Crutcher RM, Lien DJ. 1984. In *IAU Colloq. 81: Local Interstellar Medium*, ed. Y Kondo, FC Bruhweiler, BD Savage, pp. 117–21. NASA Conf. Publ. 2345
Crutcher RM, Wandelt B, Heiles C, Falgarone E, Troland TH. 2010. *Ap. J.* 725:466–79
Cummings AC, Stone EC, Steenberg CD. 2002. *Ap. J.* 578:194–210
de Geus EJ. 1992. *Astron. Astrophys.* 262:258–70
Draine BT. 2009. *Space Sci. Rev.* 143:333–45
Dupuis J, Vennes S, Bowyer S, Pradhan AK, Thejll P. 1995. *Ap. J.* 455:574
Ebel DS. 2000. *J. Geophys. Res.* 105:10363–70
Egger RJ, Aschenbach B. 1995. *Astron. Astrophys.* 294:L25–28

Esquivel A, Benjamin RA, Lazarian A, Cho J, Leitner SN. 2006. *Ap. J.* 648:1043–51

Fisk LA, Kozlovsky B, Ramaty R. 1974. *Ap. J.* 190:L35–38

Fosalba P, Lazarian A, Prunet S, Tauber JA. 2002. *Ap. J.* 564:762–72

Frisch P, York DG. 1986. In *The Galaxy and the Solar System*, ed. R Smoluchowski, JN Bahcall, MS Matthews, pp. 83–100. Tucson: Univ. Ariz. Press

Frisch PC, ed. 2006. *Solar Journey: The Significance of our Galactic Environment for the Heliosphere and Earth*, Vol. 338. Dordrecht: Springer

Frisch PC. 1981. *Nature* 293:377–79

Frisch PC. 1993. *Ap. J.* 407:198–206

Frisch PC. 1994. *Science* 265:1423

Frisch PC. 1995. *Space Sci. Rev.* 72:499–592

Frisch PC. 2003. *Ap. J.* 593:868–73

Frisch PC. 2005. *Ap. J. Lett.* 632:L143–46

Frisch PC. 2010. *Ap. J.* 714:1679–88

Frisch PC, Andersson B, Berdyugin A, Funsten HO, Magalhaes AM, et al. 2010a. *Ap. J.* 724:1473–79

Frisch PC, Bzowski M, Grün E, Izmodenov V, Krüger H, et al. 2009. *Space Sci. Rev.* 146:235–73

Frisch PC, Dorschner JM, Geiss J, Greenberg JM, Grün E, et al. 1999. *Ap. J.* 525:492–516

Frisch PC, Grodnicki L, Welty DE. 2002. *Ap. J.* 574:834–46

Frisch PC, Heerikhuisen J, Pogorelov NV, DeMajistre B, Crew GB, et al. 2010b. *Ap. J.* 719:1984–92

Frisch PC, Müller H-R. 2011. *Space Sci. Rev.* doi: 10.1007/s11214-011-9776-x

Frisch PC, Slavin JD. 2003. *Ap. J.* 594:844–58

Frisch PC, Slavin JD. 2006. See Frisch 2006, pp. 133–93

Frisch PC, York DG. 1983. *Ap. J. Lett.* 271:L59–63

Fuchs B, Breitschwerdt D, de Avillez MA, Dettbarn C, Flynn C. 2006. *MNRAS* 373:993–1003

Gloeckler G, Fisk L. 2007. *Space Sci. Rev.* 27:489–513

Grevesse N, Asplund M, Sauval AJ. 2007. *Space Sci. Rev.* 130:105–14

Gry C. 1996. *Space Sci. Rev.* 78:239–46

Gry C, Jenkins EB. 2001. *Astron. Astrophys.* 367:617–28

Grzedzielski S, Lallement R. 1996. *Space Sci. Rev.* 78:247–58

Han JL. 2006. *Chin. J. Astron. Astrophys. Suppl.* 6:211–17

Haud U. 2010. *Astron. Astrophys.* 514:Article 27

Haverkorn M, Goss WM, eds. 2007. *SINS – Small Ionized and Neutral Structures in the Diffuse Interstellar Medium. ASP Conf. Ser.* 365. San Francisco: ASP

Heerikhuisen J, Pogorelov NV, Zank GP, Crew GB, Frisch PC, et al. 2010. *Ap. J. Lett.* 708:L126–30

Heiles C. 1989. *Ap. J.* 336:808–21

Heiles C. 1998. *Ap. J.* 498:689–703

Heiles C, Troland TH. 2003. *Ap. J. Suppl.* 145:329–54

Heiles C, Troland TH. 2005. *Ap. J.* 624:773–93

Hennebelle P, Audit E. 2007. See Haverkorn & Goss 2007, p. 133

Holberg JB, Bruhweiler FC, Barstow MA, Dobbie PD. 1999. *Ap. J.* 517:841–49

Izmodenov VV. 2009. *Space Sci. Rev.* 143:139–50

Jenkins EB, Oegerle WR, Gry C, Vallerga J, Sembach KR, et al. 2000. *Ap. J. Lett.* 538:L81–85

Jenkins EB, Reale MA, Zucchino PM, Sofia UJ. 1996. *Ap. Space Sci.* 239:315–60

Jenkins EB, Tripp TM. 2007. See Haverkorn & Goss 2007, p. 51

Kalberla PMW, Kerp J. 2009. *Annu. Rev. Astron. Astrophys.* 47:27–61

Koutroumpa D, Lallement R, Raymond JC, Kharchenko V. 2009. *Ap. J.* 696:1517–25

Kwak K, Shelton RL. 2010. *Ap. J.* 719:523–39

Lallement R. 2009. *Space Sci. Rev.* 143:427–36

Lallement R, Bertin P. 1992. *Astron. Astrophys.* 266:479–85

Lallement R, Vidal-Madjar A, Ferlet R. 1986. *Astron. Astrophys.* 168:225–36

Lazarian A. 2007. *J. Quant. Spectrosc. Radiat. Transf.* 106:225–56

Lehner N, Jenkins E, Gry C, Moos H, Chayer P, Lacour S. 2003. *Ap. J.* 595:858–79

Leroy JL. 1999. *Astron. Astrophys.* 346:955–60

Leske RA. 2000. In *AIP Conf. Proc. 26th Int. Cosmic Ray Conf., ICRC XXVI*, ed. BL Dingus, DB Kieda, MH Salamon, 516:274–82. New York: AIP

Linsky JL, Draine BT, Moos HW, Jenkins EB, Wood BE, et al. 2006. *Ap. J.* 647:1106–24

Linsky JL, Rickett BJ, Redfield S. 2008. *Ap. J.* 675:413–19

Linsky JL, Wood BE. 1996. *Ap. J.* 463:254–70

Lisse CM, Dennerl K, Englhauser J, Harden M, Marshall FE, et al. 1996. *Science* 274:205–9

Mac Low M-M, Balsara DS, Kim J, de Avillez MA. 2005. *Ap. J.* 626:864–76

Mac Low M-M, McCray R. 1988. *Ap. J.* 324:776–85

Maíz-Apellániz J. 2001. *Ap. J. Lett.* 560:L83–86

Mann I. 2009. *Annu. Rev. Astron. Astrophys.* 48:173–203

McCammon D, Almy R, Apodaca E, Bergmann Tiest W, Cui W, et al. 2002. *Ap. J.* 576:188–203

McCammon D, Burrows DN, Sanders WT, Kraushaar WL. 1983. *Ap. J.* 269:107–35

McClure-Griffiths NM, Dickey JM, Gaensler BM, Green AJ. 2002. *Ap. J.* 578:176–93

McComas DJ, Allegrini F, Bochsler P, Bzowski M, Christian ER, et al. 2009a. *Science* 326:959–62

McComas DJ, Allegrini F, Bochsler P, Bzowski M, Collier M, et al. 2009b. *Space Sci. Rev.* 146:11–33

Meyer DM, Lauroesch JT, Heiles C, Peek JEG, Engelhorn K. 2006. *Ap. J. Lett.* 650:L67–70

Minter AH, Spangler SR. 1996. *Ap. J.* 458:194–24

Möbius E, Bochsler P, Bzowski M, Crew GB, Funsten HO, et al. 2009. *Science* 326:969–71

Möbius E, Bzowski M, Chalov S, Fahr H, Gloeckler G, et al. 2004. *Astron. Astrophys.* 426:897–907

Müller H-R, Frisch PC, Fields BD, Zank GP. 2009. *Space Sci. Rev.* 143:415–25

Müller H-R, Frisch PC, Florinski V, Zank GP. 2006. *Ap. J.* 647:1491–1505

Müller H-R, Zank GP. 2004. *J. Geophys. Res.* 109:7104–16

Murthy J, Henry RC, Sujatha NV. 2010. *Ap. J.* 724:1389–95

Opal CB, Weller CS. 1984. *Ap. J.* 282:445–51

Opher M, Richardson JD, Toth G, Gombosi TI. 2009. *Space Sci. Rev.* 143:43–55

Pagani L, Steinacker J, Bacmann A, Stutz A, Henning T. 2010. *Science* 329:1622–24

Paresce F. 1982. *Mem. Soc. Astron. Ital.* 53:383–409

Peek JEG, Heiles C, Peek KMG, Meyer DM, Lauroesch JT. 2011. arXiv:1104.5232

Perryman MAC. 1997. *Astron. Astrophys.* 323:L49–52

Pogorelov NV, Heerikhuisen J, Mitchell JJ, Cairns IH, Zank GP. 2009. *Ap. J. Lett.* 695:L31–34

Ratkiewicz R, Ben-Jaffel L, Grygorczuk J. 2008. In *Numerical Modeling of Space Plasma Flows*, ed. NV Pogorelov, E Audit, GP Zank, *ASP Conf. Ser.* 385:189

Redfield S. 2006. In *ASP Conf. Ser. 352: New Horizons in Astronomy, Frank N. Bash Symp. 2005*, ed. SJ Kannappan, S Redfield, JE Kessler-Silacci, M Landriau, N Drory, p. 79. San Francisco: ASP

Redfield S, Falcon RE. 2008. *Ap. J.* 683:207–25

Redfield S, Linsky JL. 2000. *Ap. J.* 534:825–37

Redfield S, Linsky JL. 2002. *Ap. J. Suppl.* 139:439–65

Redfield S, Linsky JL. 2004a. *Ap. J.* 602:776–802

Redfield S, Linsky JL. 2004b. *Ap. J.* 613:1004–22

Redfield S, Linsky JL. 2008. *Ap. J.* 673:283–314

Reynolds RJ. 2004. *Adv. Space Res.* 34:27–34

Richardson JD, Stone EC. 2009. *Space Sci. Rev.* 143:7–20

Rickett BJ. 2007. See Haverkorn & Goss 2007, p. 207

Robertson IP, Kuntz KD, Collier MR, Cravens TE, Snowden SL. 2010. *Twelfth Int. Solar Wind Conf.* 1216:532–38

Rucinski D, Cummings AC, Gloeckler G, Lazarus AJ, Möbius E, Witte M. 1996. *Space Sci. Rev.* 78:73–84

Salvati M. 2010. *Astron. Astrophys.* 513:A28–31

Santos FP, Corradi W, Reis W. 2011. *Ap. J.* 728:104–27

Savage BD, Bohlin RC. 1979. *Ap. J.* 229:136–46

Savage BD, Sembach KR. 1996. *Annu. Rev. Astron. Astrophys.* 34:279–330

Schönrich R, Binney J, Dehnen W. 2010. *MNRAS* 403:1829–33

Sfeir DM, Lallement R, Crifo F, Welsh BY. 1999. *Astron. Astrophys.* 346:785–97

Slavin JD. 1989. *Ap. J.* 346:718–27

Slavin JD. 2009. *Space Sci. Rev.* 143:311–22

Slavin JD, Frisch PC. 2002. *Ap. J.* 565:364–79

Slavin JD, Frisch PC. 2006. *Ap. J. Lett.* 651:L37–40

Slavin JD, Frisch PC. 2008. *Astron. Astrophys.* 491:53–68

Slavin JD, Frisch PC, Heerikhuisen J, Pogorelov NV, Müller H-R, et al. 2010. *Twelfth International Solar Wind Conference*. AIP Conf. Proc. 1216:497–501

Slavin JD, Shull JM, Begelman MC. 1993. *Ap. J.* 407:83–99

Smith RK, Cox DP. 2001. *Ap. J. Suppl.* 134:283–309

Snowden SL, Cox DP, McCammon D, Sanders WT. 1990. *Ap. J.* 354:211–19

Snowden SL, Egger R, Finkbeiner DP, Freyberg MJ, Plucinsky PP. 1998. *Ap. J.* 493:715–29

Sofia UJ, Jenkins EB. 1998. *Ap. J.* 499:951–65

Spangler SR, Savage AH, Redfield S. 2010. *Nonlinear Process. Geophys.* 17:785–93

Tinbergen J. 1982. *Astron. Astrophys.* 105:53–64

Vallerga J. 1998. *Ap. J.* 497:921–27

Vallerga JV, Vedder PW, Craig N, Welsh BY. 1993. *Ap. J.* 411:729–49

van de Hulst HC, Reesinck JJM. 1947. *Ap. J.* 106:121–27

Vergely J, Valette B, Lallement R, Raimond S. 2010. *Astron. Astrophys.* 518:A31–41

Vogt SS, Butler RP, Rivera EJ, Haghighipour N, Henry GW, Williamson MH. 2010. *Ap. J.* 723:954–65

Warwick RS, Barber CR, Hodgkin ST, Pye JP. 1993. *MNRAS* 262:289–300

Washimi H, Tanaka T. 1996. *Space Sci. Rev.* 78:85–94

Welsh BY, Lallement R, Vergely J, Raimond S. 2010a. *Astron. Astrophys.* 510:Article 54

Welsh BY, Wheatley J, Siegmund OHW, Lallement R. 2010b. *Ap. J. Lett.* 712:L199–202

Welty DE, Hobbs LM, Lauroesch JT, Morton DC, Spitzer L, York DG. 1999. *Ap. J. Suppl.* 124:465–501

Witt AN, Gold B, Barnes FS III, DeRoo CT, Vijh UP, Madsen GJ. 2010. *Ap. J.* 724:1151–60

Witte M. 2004. *Astron. Astrophys.* 426:835–44

Wolff B, Koester D, Lallement R. 1999. *Astron. Astrophys.* 346:969–78

Wolleben M. 2007. *Ap. J.* 664:349–56

Wood BE. 2004. *Living Rev. Solar Phys.* 1:2

Wood BE, Linsky JL, Zank GP. 2000. *Ap. J.* 537:304–11

Wood BE, Redfield S, Linsky JL, Müller H-R, Zank GP. 2005. *Ap. J. Suppl.* 159:118–40

Wood BE, Redfield S, Linsky JL, Sahu MS. 2002. *Ap. J.* 581:1168–79

York DG, Kinahan BF. 1979. *Ap. J.* 228:127–46

Zank GP. 1999. *Space Sci. Rev.* 89:413–688

Contents